Collective transitions from orbiting to matrix invasion in three-dimensional multicellular spheroids

Jiwon Kim,[1] Hyuntae Jeong,[1] Carles Falcó,[2] Alex M. Hruska,[1] W. Duncan Martinson,[3] Alejandro Marzoratti,[1] Mauricio Araiza,[4] Haiqian Yang,[5] Vera C. Fonseca,[6] Stephen A. Adam,[7] Christian Franck,[4] José A. Carrillo,[2] Ming Guo,[5] and Ian Y. Wong[1,6,*]

[1] *School of Engineering, Legoretta Cancer Center. Brown University. 184 Hope St Box D, Providence RI 02912, USA*
[2] *Mathematical Institute, University of Oxford, Oxford, OX2 6GG, United Kingdom*
[3] *The Francis Crick Institute, 1 Midland Road, London, NW1 1AT, United Kingdom*
[4] *Department of Mechanical Engineering. University of Wisconsin-Madison. 1513 University Ave, Madison, WI 53706, USA*
[5] *Department of Mechanical Engineering, Massachusetts Institute of Technology, 77 Massachusetts Avenue, Cambridge, Massachusetts 02139, USA*
[6] *Department of Pathology & Laboratory Medicine, Brown University. Box G-B377, Providence RI 02912, USA*
[7] *Department of Cell and Developmental Biology, Northwestern University. 320 E. Superior Street. Chicago, IL 60611, USA*

(Dated: January 27, 2026)

Coordinated cell rotation along a curved matrix interface can sculpt epithelial tissues into spherical morphologies. Subsequently, radially oriented invasion of multicellular strands or branches can occur by local remodeling of the confining matrix. These symmetry-breaking transitions emerge from the dynamic reciprocity between cells and matrix but remain poorly understood. Here, we show that epithelial cell spheroids collectively transition from circumferential orbiting to radial invasion via bidirectional interactions with the surrounding matrix curvature. Initially, spheroids exhibit an ellipsoidal shape but become rounded as orbiting occurs. In turn, orbiting along sharper curvature results in locally stronger contractile tractions, which gradually align collagen fibers in the radial direction. Thus, the initially elongated morphology primes the matrix towards subsequent invasion of two to four strands that are roughly aligned with the major axis. We then show that orbiting can be arrested and invasion can be reversed using osmotic pressure. We also investigate coordinated orbiting in mosaic spheroids, showing a small fraction of cells with weakened cell-cell adhesions can impede collective orbiting but still invade into the matrix. Altogether, this work elucidates how symmetry-breaking in tissue morphogenesis is governed by the interplay of collective migration and the local curvature of the cell-matrix, with relevance for embryonic development and tumor progression.

INTRODUCTION

Collective cell migration within a spherical geometry can occur along circumferential or radial directions, shaping tissue morphology via coordinated orbiting or matrix invasion [1]. For instance, normal epithelial cells undergo coherent rotational motions to organize spherical acini or alveoli when embedded within 3D matrix [2–8]. Moreover, follicle epithelial cells drive global egg chamber rotation within a basement membrane during *Drosophila* oogenesis [9, 10]. Analogous rotational motions have been observed when epithelial cells are confined in planar geometries within circular corrals [11–14] or migrate along cylindrical geometries [15]. In these scenarios, circumferential migration is guided by the curvature of the confining material, which remains largely static since cells cannot alter the local curvature. Thus, the effect of dynamic reciprocity, whereby cell migration is shaped by the matrix interface and the matrix interface is (in turn) shaped by cell migration, remains poorly understood.

Multicellular spheroids can also invade into the surrounding matrix by opening up cell-sized gaps using matrix metalloproteinases (MMPs) and / or irreversible remodeling via actomyosin contractility [16–25].

* Contact: ian_wong@brown.edu

Such invasion may be facilitated by a fast orbiting subpopulation with enhanced capabilities for path generation or coordination of followers [18–20, 24–26]. Such highly motile phenotype may be a consequence of the epithelial-mesenchymal transition (EMT), which is associated with a weakening of cell-cell adhesions, as well as front-back polarity with vimentin expression and strengthened cell-matrix adhesions [27]. Indeed, in heterogeneous populations, cells with more mesenchymal states may sort away from cells with more epithelial states based on differences in cell-cell adhesion (e.g., E-cadherin). Historically, cell sorting was studied using embryos and spheroids in the absence of exogenous matrix [28]. Nevertheless, cell sorting can be further mediated by differences in both cell-cell and cell-matrix adhesion when spheroids are embedded in 3D matrix [26, 29]. Computational models based on self-propelled particles with varying adhesion [30] can exhibit such self-sorting [31, 32], as well as coordinated migration behaviors (also described as flocking or milling) [33–35].

Here, we show that multicellular spheroids of mammary epithelial cells transition from collective orbiting to strand invasion based on dynamic mechanical interactions with the surrounding 3D matrix. Initially, multicellular spheroids are slightly ellipsoidal but become rounded due to coordinated rotational motion along the curved matrix interface. This occurs since cell-generated tractions near regions of sharper curvature drive stronger radial matrix deformations along the initial elongation axis. Subsequently, localized collagen fiber alignment disrupts collective orbiting, promoting strand invasion at a few locations roughly aligned with the initial elongation axis of the spheroid. We reversibly manipulate these interfacial dynamics using osmotic pressure, which can drive retraction of strands back into the spheroid, as well as reversibly arrest orbiting. Further, we examine whether heterogeneous "mosaic" spheroids continue to orbit and invade when mammary epithelial cells are mixed with increasing fractions of EMT-induced mammary cells with weakened cell-cell adhesion. Finally, we develop an agent-based model that recapitulates collective transitions from orbiting to invasion based on geometric perturbations of local boundary curvature at a few discrete locations. Overall, this work reveals the dynamic interplay of collective migration and local curvature at a spheroid-matrix interface, with implications for epithelial tissue morphogenesis in development and disease.

RESULTS

Multicellular Spheroids Transition from Orbiting to Invasion in Collagen I Matrix

We investigated transitions between different collective cell migration modes using multicellular spheroids of mammary epithelial cells (MCF-10A) embedded within 3D collagen I hydrogels. Briefly, hanging drop culture was used to aggregate ∼500 cells into spheroids of ∼150 μm in diameter, which were then embedded in 6 mg/mL bovine collagen I for live cell imaging (Fig. S1A-F), which exhibits a typical fiber spacing of 0.7 μm and stiffness of $E = 130 \pm 40$ Pa by atomic force microscopy (Fig. S1G-M). MCF-10A cells were stably transfected so that their nuclei were fluorescent (H2B-mCherry) and imaged using spinning disk confocal microscopy in an environmentally controlled chamber.

Cells within the spheroid exhibited collective orbiting motions within 6 h of embedding, continuing for the next 6 h (Fig. 1A, i-iv; Mov. S1). Coordinated rotational motion primarily occurred in the focal plane based on 3D tracking of representative nuclei (Fig. S2), so we primarily analyzed cell motion within the equatorial plane of the spheroid. We visualized rotational motion by unwrapping 20 μm-thick concentric layers of cell (nuclei) at sequential time points as a kymograph (Fig. 1BC; S3AB). During the first 6 hours, the cell nuclei trajectory stayed parallel and horizontal, representing that the relative angular location of the cells were largely unchanged (Fig. 1C, i-ii; S3CE). Subsequently, the parallel upward trajectories from 6–12 h indicate highly coordinated angular motion within the outermost layer (Fig. 1C, ii-iv; S3CE). Finally, cell nuclei exhibited flat trajectories in the kymograph through the next 24 h, indicating that their angular positions within the outermost layer remained relatively consistent (Fig. 1C, iv-vi; S3CE, Post-orbiting). Sustained circumferential velocity fields mostly occurred in the outermost 40 μm of the spheroid, and were less pronounced in the innermost 50 μm of the core (Fig. 1D, ii-iv; Mov. S2). In comparison, the radial components of the velocity were relatively uncorrelated and sporadic from 0-11 h (Fig. 1E, i-iv; S3DF, Pre-orbiting, Orbiting). However, cells located at the top and lower left of the spheroid veered radially after 12 h, disrupting circumferential migration (Fig. 1A, v; S3DF, Post-orbiting). Indeed, "hotspots" of increased radial velocity were observed at 17 h, localized at the top and lower left (Fig. 1E, v; S3F). The spheroid

morphology at the top and lower left became slightly sharper relative to the otherwise rounded periphery elsewhere. Subsequently, multicellular strand invasion was observed at the top and lower left by 24.75 h (Fig. 1A, vi), also associated with increased radial velocities (Fig. 1E, vi).

The beginning and end of the orbiting phase were determined by a peripheral coordination parameter $D = \text{sgn}(\langle \hat{\mathbf{r}} \times \hat{\mathbf{v}} \rangle)$, which describes the fraction of velocity pixels oriented circumferentially in the outermost region (Fig. 1F). We empirically set a threshold of D greater than 0.5 for coordinated orbiting. From 6-12 h, $D \approx 0.7$, indicating the high fraction of pixels within the designated peripheral area oriented to the primary orbiting direction (Fig. 1G, ii-iv). After 12 h, D decreased in magnitude with fluctuations comparable to the pre-orbiting period (Fig. 1G, iv-v). Spheroid area remained roughly constant during orbiting but increased dramatically when invasion occurred via multicellular strands (Fig. S3GH).

Curvature of Spheroid-Matrix Interface Shapes Collective Migration Mode

Next, we investigated how collective migration was shaped by the local curvature along the spheroid periphery, based on our observation that radial invasion proceeded from sharp outgrowths that perturbed the locally rounded morphology. Unexpectedly, we observed that most spheroids were ellipsoidal in the hanging drop and remained so after being embedded in collagen I (Fig. S1B-F). As a representative example, the spheroid was slightly elongated along the vertical axis from 0-3 h, which we quantified based on the radial deviation from an equivalent reference circle defined as a circle with the same area and centroid as the spheroid cross-section. The reference radius, r_{ref}, is defined as radius of the equivalent circle, given by $\sqrt{\frac{\text{area}}{\pi}}$. For each boundary point, r denotes the centroid-to-boundary distance, and the radial deviation is quantified as $\Delta r = r - r_{ref}$. For convenience, $\theta = 0°$ was set at the position of maximum protrusion at time = 0 h, where $\Delta r = 8$ μm (Fig. 2AB, i). This spheroid was also slightly flattened (laterally) with Δr = -3 μm on the left and right ($\theta = \pm 90°$). The spheroid became more rounded as orbiting commenced, so that the radial deviation decreased to $\Delta r = 0$ μm at $\theta = 0°$ and to $\Delta r = 1$ μm at $\theta = \pm 90°$ from 8.5-10.5 h (Fig. 2AB, ii). We further quantified this based on roundness ($\frac{4 \times \text{area}}{\pi \times (\text{major axis})^2}$), which is 1 for a perfect circle and approaches 0 for non-circular shapes. The spheroid roundness varied from 0.9 prior to orbiting (0-6 h), up to almost 1.0 during orbiting (6-12 h) (Fig. 2C, i-ii; Mov. S3). Typically, orbiting began at 5 ± 2 h and completed at 13 ± 2 h, lasting about 7.5 hours (Fig. 2D). However, the corresponding compaction of the spheroid shape, defined as the duration during which the roundness ranks in the top 10% within the first 24 hours, was observed slightly later, from 8 ± 3 h to 16 ± 3 h, lasting for 9 hours. Thus, coordinated orbiting was typically observed before rounding of the spheroid, implying a role in subsequent morphological changes. As the spheroid transitioned to matrix invasion after 12 h, there was a gradual increase in locally sharpened features near $\theta = 0°$ and 180° (Fig. 2AB, iii). This "roughening" of the periphery corresponded to a decrease of roundness to 0.8 (Fig. 2C, iii). Further, the invasion of multicellular strands from these angular locations corresponded to the increasing local curvature near $\theta = 0°$ and 180° at 36-39 h (Fig. 2AB, iv) and a further decrease in roundness to 0.5 (Fig. 2C, iv). Remarkably, the angular locations of invasive strands were highly correlated with the initially protruded poles of the spheroids (Fig. 2B, i, iii-iv). The angular positions of the local maxima in Δr at 0 h and 48 h differed on average by only $\Delta\theta = -5 \pm 23°$ (Fig. 2E). Further, spheroids typically exhibited 2-4 invasive strands, aligned roughly with the initial elongation axis (Fig. 2F-I).

Since the multicellular spheroid was adherent to collagen I, it was hypothesized that alterations in spheroid morphology were driven by cell-generated forces that were deforming the surrounding 3D matrix. Optical flow was used to track the temporal displacement of matrix-embedded tracer particles every 15 minutes (Fig. 3A; S4). As cells migrated circumferentially along the spheroid periphery, transient hotspots of radial ECM displacement emerged and disappeared at various positions along the boundary, indicating that cell-generated tractions that were spatially non-uniform (Fig. 3A, ii-iv; Mov. S4). Some cells were initially more migratory than others, "steering" the coordinated orbiting (Fig. S5A). Indeed, these highly migratory "steering" cells exerted strong tractions on the matrix, as evidenced by large matrix displacements towards these cells, opposite to the direction of cell migration (Fig. S5BC). However, matrix displacements near the initially elongated regions (at the top and bottom) were stronger and oriented radially inward, relative to the negligible matrix displacements near the flattened regions (at the sides) (Fig. S5B-E). We then visualized

whether matrix deformations were sustained over time by analyzing the cumulative particle displacements relative to their initial positions at $t = 0$. At 6 h after embedding, spheroids exhibited slightly increased inward tractions localized at the top and bottom relative to the rest of the periphery (Fig. 3B, ii), consistent with slight flattening at these locations (Fig. 2A, ii). During collective orbiting from 6-12 h, the spheroid exhibited a further increase in inward tractions at the top and bottom (Fig. 3B, iii-iv; Mov. S5), even as the rounding of the boundary was nearly complete (Fig. 2A-C, ii). To visualize these locally non-uniform matrix deformations, we modified our previous DART protocol to bin the displacement field at discrete angular positions [36]. Notably, this analysis indicates the increased matrix displacements at the $\theta = 0°$ and 180° of the spheroid from 6–9 h, which remain comparable until 12 h (Fig. 3C, ii-iii; D). Moreover, there were subtle protrusive tractions at $\pm 90°$, consistent with slight rounding (Fig. 3C, ii-iv). The following transition to invasion after 12 h was associated with monotonically increasing contractile tractions near 0° and 180° (Fig. 3B-D). Finally, confocal reflectance imaging indicated local collagen fiber alignment at these sites of large matrix displacement (Fig. 3E-H).

Altogether, these experimental results indicate a complex interplay between local curvature, collective orbiting, and matrix deformation. We observe that "steering" cells at varying angular locations initiate collective migration (Fig. S5A), likely via a contact guidance mechanism along sharply curved interfaces. These cells exert localized tractions at their leading and trailing edges, which result in matrix displacements in varying directions depending on angular cell position. For example, the leading edge of a fast-moving cell moving from 90° to 180° applies tractions that pull the matrix toward it (Fig. 3I). The resulting displacement vector of a tracer particle can be decomposed into a circumferential component tangent to the spheroid and oriented towards the cell, as well as a radial component oriented towards the spheroid (as observed in Fig 3A). As this cell moves onward along the periphery (e.g., continuing from 180° to -90°), the same bead experiences tractions applied by the trailing edge instead of the leading edge. Consequently, the circumferential component of bead displacement is reversed to align with the cell migration direction, while the radial component remains oriented toward the spheroid. As cells traverse regions of sharper curvature, their tractions act more strongly in the radial direction relative to regions of flatter curvature, driving the compaction of the spheroid into a rounder morphology along the initial elongation axis (Fig. 3BCD, S5BCDE). Such shear stresses applied to fibrous materials such as collagen can result in negative normal stresses (acting radially here) [37], which may enhance these geometric effects. Over time, the continuous application of radial stress results in radial alignment of collagen fibers (Fig. 3E-H). This drives a dynamic reciprocity where the radial fiber alignment reorients cell polarity so that they are steered radially outward, disrupting coordinated orbiting and biasing towards radial invasion. Indeed, spheroids consisting of MCF-10A cells labeled with fluorescent SiR-actin exhibited protrusive outgrowths at invasion sites along the elongation axis (Fig. S6). Further, dual labeling of these MCF-10A with mEmerald-vimentin revealed localized expression at some invasion sites, suggestive of leader cells and EMT.

We further verified this mechanism by systematically varying spheroid size and aspect ratio (Fig. S7, S8, Mov. S6). Small spheroids (250 cells) exhibit initially sharper curvature, corresponding to highly coordinated orbiting. However, these smaller spheroids are also less elongated, so the boundary retraction is smaller, and the subsequent invasion is limited (Fig. S7A-D, S8). In comparison, large spheroids (1500 cells) initially show shallower curvature, and there are only sporadic patches of coordinated migration at the ends (Fig. S7E-H). However, larger spheroids are more elongated, resulting in larger boundary retraction, which corresponds to stronger tractions and greater matrix invasion (Fig. S8). Finally, elongated spheroids (500 cells, 220 μm long but 100 μm wide) exhibit initially sharp curvature at the ends but relatively flat sides. As a consequence, sporadic collective migration is again localized at the ends and not at the sides. However, there is an even larger aspect ratio change in elongated spheroids relative to large spheroids, which results in strong tractions and matrix invasion near poles (Fig. S7 IJKL, Fig. S8). Overall, these trends show the transition from orbiting to invasion is governed by competing trends in spheroid size: increasing spheroid size results in decreasing local curvature and coordinated orbiting, but also greater boundary retraction which generates stronger localized tractions that eventually drive matrix invasion (Fig. S8L).

Reversible Suppression of Collective Migration by Osmotic Pressure

We then sought to manipulate collective migration by applying osmotic pressure to perturb cellular outgrowths at the spheroid periphery. Cell culture media was supplemented with 4% polyethylene glycol 400 Da (PEG400) to increase the osmolality, which resulted in a volumetric compression (Fig. 4, S9). For example, multicellular spheroids in the control condition with normal (isotonic) media exhibited the usual orbiting for 1 day, followed by a transition to invasion over the next 4 days (Fig. 4ACD, S9AEFG; Mov. S7). In comparison, spheroids continuously treated with PEG400 over 5 days maintained a circular morphology with roughly constant size (Fig. 4BEF, S9B; Mov. S7). Moreover, cell migration was largely arrested, with minimal coordination and tractions (Fig. S9HIJ, S10A, S11).

Further, we investigated whether this suppression of collective migration by osmotic pressure was reversible. First, multicellular spheroids were cultured for 2 days in normal media, exhibiting the usual circumferential orbiting on day 1 and radial invasion on day 2. With the addition of PEG400-supplemented media, matrix invasion was arrested. Remarkably, the multicellular strands gradually retracted back into the spheroid over the next 2 days, and the spheroid was roughly spherical by day 5 (Fig. 4G, S9CKM; Mov. S8). This switch from normal media to PEG400 after day 2 resulted in a monotonic decrease in projected area and traction, along with increase in circularity, which was the opposite of the control condition (Fig. 4C,D, S10B). As the strand retracted inward, the matrix-embedded tracer particles were displaced away from the spheroid, consistent with a relaxation of matrix tension due to the weakening of cell-generated tractions (Fig. S10F).

It should be noted that these spheroids did not exhibit any orbiting motion at day 5, indicating that collective migration was largely arrested by osmotic pressure, consistent with the spheroids continuously treated with PEG400 (Fig. S9KLM). Spheroids initially treated with PEG400 for 2 days remained compact in size for another 2 days, even after the media was changed to isotonic condition(Fig. 4EFH, S9D; Mov. S8). Nevertheless, orbiting was observed on day 4, representing a delayed onset relative to the control condition (Fig. S9NOP). In accordance with previous results, inward traction increased as the spheroid orbiting motion initiated (Fig. S10CE). By day 5, spheroid showed sudden matrix invasion, leading to a significant increase in spheroid area (Fig. 4FH, S9D). Thus, this switch from PEG400 to normal media after day 2 led to a slight increase in projected area only on day 5, along with a sizable decrease in circularity. Thus, transient osmotic pressure can delay collective orbiting and even reverse matrix invasion of 3D multicellular spheroids.

Increasing Heterogeneity Disrupts Collective Orbiting but not Radial Invasion

We next explored whether differential cell-cell adhesion would affect collective orbiting or matrix invasion through the addition of a second cell type (also MCF-10A), which could be induced prior to spheroid formation to undergo the epithelial-mesenchymal transition (via Snail1), downregulating cell-cell adhesion and upregulating vimentin intermediate filament expression [38]. Fluorescently labeled MCF-10A Snail cells were mixed with MCF-10A wildtype (WT) cells at varying ratios at constant total cell numbers in the hanging drop to generate "mosaic" spheroids, then embedded in collagen matrix as before.

Spheroids with 10% Snail cells exhibited collective orbiting followed by matrix invasion (Fig. 5ABC; Mov. S9), comparable to the wholly WT spheroids (Fig. 1AB). Remarkably, both Snail and WT cells at the periphery exhibited coordinated orbiting (Fig. 5D). Subsequently, some Snail cells localized at the tips of invasive strands, suggestive of "leader cells" (Fig. 5E). Matrix displacements were comparable for mosaic spheroids with 10% Snail and wholly WT spheroids (Fig. S12A). In comparison, spheroids with 30% Snail cells did not exhibit collective orbiting (Fig. 5FGHI; Mov. S10). 30% Snail spheroids did exhibit several invasive strands, often led by Snail cells (Fig. 5J). Matrix displacements increased continuously over time for 30% Snail mosaic spheroids (Fig. S12B). Interestingly, when compared to the WT 100% and Snail 10% mosaic spheroids, the 30% mosaic spheroid invaded the most (Fig. S14), perhaps due to cooperativity between Snail cell "leaders" and WT "followers."

Finally, spheroids composed of 100% Snail cells maintained a rounded morphology over 48 h, with negligible collective migration, either circumferential or radial (Fig. S13) with very weak inward and outward matrix displacements (Fig. S12C). This suggests that individual MCF-10A Snail cells are unable to sufficiently deform and remodel the surrounding collagen I for invasion, perhaps lacking sufficiently strong cell-cell

adhesions for coordinated contractility.

We further perturbed MMP activity by treating with a broad spectrum MMP inhibitor (GM6001) compared to DMSO as a vehicle control. 100% WT spheroids after GM6001 treatment exhibited clockwise orbiting from 6-30 h, with a gradual reversal towards counter-clockwise orbiting that continued through 48 h (Fig. S15, Mov. S11). Moreover, these spheroids became more circular after 12 h, but maintained this rounded morphology through the next 5 days (Fig. S15 A, E-I). We also treated mosaic spheroids of 30% Snail and 70% WT cells with GM6001. By day 5, cell sorting between Snail and WT cells gave rise to two different types of invading strands, which are WT-only strands (thick), and Snail-only strands (thin). Both types of strands were consistently observed in both DMSO control and GM6001 treated conditions, with shorter strands observed after GM6001 treatment (Fig. S15JK).

These results show that collective orbiting is impeded by increasing heterogeneity. Nevertheless, spheroids that do not orbit can still collectively invade if sufficient matrix remodeling occurs (30% Snail). Inhibition of MMP activity sustains orbiting in WT spheroids, but impedes collective invasion of both WT and Snail cells.

Cellular Adhesions and Boundary Geometry Govern Coordinated Orbiting in a Computational Model

To further elucidate how collective orbiting was mediated by interactions between cells and a curved ECM boundary, we developed a computational model with tunable interactions and analyzed how geometric perturbations to this system affected the stability of coordinated migration. Cells were treated as active, self-propelled agents that interact via soft repulsion at short distances and adhesion-based attraction at longer distances [33, 39, 40]. Collective orbiting ("milling") can emerge in the absence of boundaries when their cell-cell forces are defined by certain potentials [35]. Nevertheless, here we further implement an ECM boundary as a set of discrete equally spaced particles that surround the cells. In order to follow a curved boundary, cells were polarized with an orientation axis and can only adhere to ECM particles within a certain angular range of this axis ($\pm 60°$). Further, cells exhibit a short-range soft repulsion from ECM particles that is analogous to their interaction with nearby neighboring cells. Since we aimed to understand how the interplay of cell-cell and cell-matrix forces influences collective orbiting, we made the simplifying assumption that all ECM particles were static to eliminate potentially confounding effects from dynamic boundaries.

We systematically varied parameters associated with cell-cell and cell-matrix adhesion forces acting on cells confined within a perfect circular boundary to evaluate how these interactions (de)stabilize collective orbiting over long time periods. We evaluated the impact of these changes by measuring a global coordination parameter based on the average normalized angular momentum, $\langle L \rangle$, which has a value of 1 for perfectly coordinated angular motion and 0 for random migration over the entire area. We found migration was arrested in the limit of weak cell-matrix adhesion and strong cell-cell adhesion (Fig. 6AB, S16). Globally coordinated orbiting occurred in an intermediate regime with slightly stronger cell-matrix adhesion and slightly weaker cell-cell adhesion. Further increases in the cell-matrix adhesion strength parameter resulted in peripheral orbiting of the outermost layers but uncoordinated migration of interior cells (Fig. 6AB, Mov. S11).

We then considered the stability of collective orbiting to geometric perturbations of the boundary. Collective orbiting was relatively stable to one outward perturbation, since cells migrated by following the circular boundary and detoured around misaligned cells at the perturbation site (Fig. 6CD). However, two sharp features with height h_p greater than one cell diameter and width k_p greater than two cell diameters were sufficient to destabilize collective orbiting (Fig. 6EF, Mov. S12). Cells now encountered multiple obstacles and had shorter lengths of continuously curved boundary to follow. The number and size of these boundary perturbations were consistent with our experimental observations (Fig. S17).

Finally, we analyzed collective orbiting in a mixture of two cell types with distinct adhesion properties. Snail cells were implemented with weaker cell-cell adhesion and stronger cell-matrix adhesions than WT cells, as well as isotropic sensing of the matrix. We observed that collective orbiting was robust to relatively small fractions of Snail cells (up to $\sim$10%), since WT cells at the periphery could orbit by migrating around the Snail cells at the periphery (Fig. 6GH, Mov. S13). However, initializing simulations with greater Snail cell fractions caused the cell-matrix interface to become fully occupied by Snail cells, which impeded

the ability of WT cells to migrate along the boundary. Overall, these simulations demonstrate the role of boundary curvature for coordinated orbiting with comparable cell-cell and cell-matrix adhesion. Further, an increasing fraction of obstructionist cells that occupy the boundary can also destabilize collective orbiting (see Appendix and Fig. S18-30 for further details).

DISCUSSION AND CONCLUSION

Symmetry breaking of a spherical epithelial tissue into an elongated ellipsoid or branched architectures is crucial for embryonic development and tumor progression. For example, Drosophila egg chambers elongate via global rotation and basement membrane deposition [9, 10]. Moreover, solid tumors often exhibit ellipsoidal morphologies, which has been attributed to asymmetric stress distribution in a surrounding stiff matrix [41, 42]. Finally, mammary organoids transition from cylindrical branches to spherical alveoli when the local "surface tension" switches from axial to circumferential, stabilized by collective rotation [6]. Recent live imaging of organoids has revealed the importance of rotational motion to sense local curvature and regulate cell fate decisions [6, 43]. Here, we show that that epithelial cells are exquisitely sensitive to local curvature, so that distal sites along the initial elongation axis are primed for matrix remodeling via coordinated orbiting. Thus, small perturbations that roughen the matrix interface could destabilize (mammary) gland architecture towards subsequent strand invasion at discrete sites, analogous to past work using micropatterned tumors with sharpened features [44]. Further, we investigate how collective orbiting, but not matrix invasion, is destabilized by increasing heterogeneity in the motile units via the epithelial-mesenchymal transition (EMT), which promotes a pro-invasive "leader cell" state and vimentin expression [27]. Notably, vimentin expression is associated with narrower invasive strands (Fig. S6B), suggesting it may enhance protrusive activity (e.g. invadopodia) [25]. It is intriguing to think that such orbiting to invasion behavior might occur at a primary tumor site prior to dissemination of circulating tumor cell clusters with a mixture of EMT states [45], or during the colonization of a metastatic niche.

We further demonstrate that the transient application of osmotic pressure can transiently arrest or even reverse collective invasion via a purely physiochemical mechanism. Such remote control of cell migration processes typically requires optogenetic or pharmacological manipulations of biochemical signaling [46]. It has been reported elsewhere that osmotic pressure promotes actomyosin contractility via Rho/ROCK signaling, along with stress fiber disassembly [47], which could overwhelm existing cell-matrix adhesions, pulling the invasive strands back into the spheroid. We envision that this mechanical approach for dynamically programming morphogenesis will enable exquisite control of engineered tissue formation for biomanufacturing and regenerative medicine.

Finally, the role of confinement in shaping self-organization and emergent phenomena is a profound question in active and living matter [48]. Motile units such as animal cells or swimming microorganisms confined within curved boundaries exhibit coordinated rotational motion. Recent work has examined static confinement, where pattern formation is specified and maintained by the boundary conditions. Here, we investigate a richer system with dynamic feedback between cells and the confining matrix. We implemented a computational model of self-propelled particles with tunable cell-cell and cell-matrix interactions confined within an arbitrary geometry. Our model shows that orbiting is robust when cell-cell and cell-matrix adhesions are comparable, with few sharp boundary perturbations and mostly wildtype cells. The computational results are in agreement with the experimental observations, but we acknowledge several simplifying assumptions. We treat the boundary as fixed and rigid since cell migration occurs on considerably faster timescales than matrix remodeling and proliferation, for example. computational results thus represent a limiting case for finding parameter regimes where coordinated orbiting can occur robustly. Nevertheless, future modeling could incorporate dynamic reciprocity between cells and matrix [49–51], as well as proliferation [52].

In conclusion, we show that dynamic reciprocity between multicellular spheroids and the surrounding matrix drive a transition from coordinated orbiting to strand invasion. We observed that spheroids were initially ellipsoidal, but became more rounded during circumferential orbiting. This "flattening" of the spheroid along the major axis corresponded to locally increased matrix deformation and remodeling, which are subsequently locations of multicellular strand invasion in the radial direction. We show that these orbiting and invasion dynamics are transiently arrested or reversed through the application of osmotic pressure. Moreover, we demonstrate that both orbiting and invasion can occur in mosaic spheroids with a small fraction

of EMT-induced cells. Nevertheless, an increasing fraction of EMT-induced cells will impede orbiting but facilitate matrix invasion. Lastly, we implement a minimal physical model to elucidate the interplay of cell-cell and cell-matrix adhesion with local curvature in maintaining collective orbiting. Ultimately, this spherical symmetry-breaking mechanism via a collective transition from circumferential to radial motility has potential relevance for epithelial tissue morphogenesis towards more topologically complex architectures via local budding and branching.

ACKNOWLEDGMENTS

We thank S.E. Leggett, R.E. Baker, J. Notbohm, D. Bhaskar, J. Yang, and A. McGhee for helpful conversations, as well as J.S. Brugge and D.A. Haber for the gift of stably transfected MCF-10A cell lines. IYW and JAC also thank P. Kulesa and P. Maini for catalyzing this collaboration. We acknowledge funding from Brown University's Hibbitt Engineering Postdoctoral Fellowship (JK), NIH R01GM140108 (JK, HJ, AMH, AM, HY, SAA, MG, IYW), "la Caixa" Foundation Fellowship 100010434 with code LCF/BQ/EU21/11890128 (C. Falcó), EPSRC grant EP/R014604/1 (C. Falcó, WDM, JAC), ERC Horizon 2020 Research and Innovation Program Advanced Grant Non-local-CPD 883363 (WDM, JAC), ONR Panther Award N000142212828 (MA, C. Franck), MIT School of Engineering Takeda Fellowship (HY), and ARO W911NF2310385 (IYW). WDM and JAC would also like to thank the Isaac Newton Institute for Mathematical Sciences, Cambridge, for support and hospitality during the program "Mathematics of movement: an interdisciplinary approach to mutual challenges in animal ecology and cell biology", where work on this paper was undertaken.

AUTHOR CONTRIBUTIONS

IYW conceived and supervised the project. JK and IYW designed experimental work. JK, AMH, and AM performed spheroid experiments. JK, HJ, MA, C. Franck, and IYW analyzed collective migration and tractions. JK, HY, VCF and MG characterized matrix architecture and rheology. SAA contributed cell lines. C. Falcó, WDM, JAC and IYW designed computational and theoretical work. C. Falcó and WDM implemented theoretical model and performed simulations. JK, HJ, C. Falcó, WDM, and IYW wrote the manuscript with feedback from all authors.

COMPETING INTERESTS

The authors declare no competing interests

MATERIALS AND METHODS

Cell Culture

Human mammary epithelial cells (MCF-10A), stably transfected with H2B-mCherry as a fluorescent nuclear marker were a generous gift from M.R. Ng and J.S. Brugge (Harvard Medical School). MCF-10A cells stably transfected with mEmerald-vimentin were provided by S.A. Adam (Northwestern University). Briefly, MCF-10A cells were grown on standard tissue culture T-75 flasks in a 5% CO_2 humidified incubator at 37 °C. The growth medium is composed of DMEM/F12 (Invitrogen, 11965-118) supplemented with 5% horse serum (Invitrogen, 16050-122), 20 ng/mL epidermal growth factor (R&D Systems, 236-EG), 10 μg/mL insulin (Sigma Aldrich, I-1882), 0.5 μg/mL hydrocortisone (Sigma Aldrich, H-0888), 100 ng/mL cholera toxin (Sigma Aldrich, C-8052), and penicillin streptomycin (Invitrogen No. 15070-063). An EMT-inducible MCF-10A variant, stably transfected with an 4-hydroxy-tamoxifen (4-OHT) inducible Snail expression construct fused to an estrogen receptor element response element (ER-Snail-1^{6SA}), was a generous gift from D. A. Haber (Massachusetts General Hospital) [38]. The Snail-1^{6SA} variant is refractory to phosphorylation and

is thus stably expressed and localized in the nucleus, where it initiates EMT induction. This cell line also overexpresses fluorescent proteins in the nucleus (mCherry-H2B) and cytoplasm (GFP) for live cell tracking. MCF-10A were induced for Snail expression and EMT by treatment with 500 nM OHT in growth media for 72 h.

Multicellular Spheroid Preparation in Hanging Drops

Multicellular spheroids were prepared using a modified hanging drop method. Briefly, single cell suspensions of MCF-10A were diluted to 20,000 cells/mL with methycellulose (MethoCel(R) A4M, Sigma Aldrich, 94378) at a final concentration of 1 mg/mL to promote spheroid aggregation. 25 μL droplets (500 cells each) were then dispensed onto Petri dish lids using a multichannel pipettes. These lids were gently flipped over above dishes containing 8 mL of PBS supplemented with 1% penicillin streptomycin. After 48 h, the cells aggregated into multicellular spheroids and could be isolated for further investigations. Most experiments were conducted using MCF-10A-H2B-mCherry cells. Mosaic spheroids were prepared by mixing OHT-treated MCF-10A-ER-Snail-1^{6SA} at 10%, 30% or 100% of total cell count, with the remainder being MCF-10A-H2B-mCherry cells. The size of spheroids were controlled by adjusting the number of cells per droplet. Small, medium (control), and large spheroids consisted of 250, 500, and 1500 cells, respectively. Elongated spheroids also consisted of 500 cells. However, the droplets were placed within elliptical wells in a 2 mm-thick PDMS layer on the Petri dish lid. The wells were created using a by punching with a flattened 5 mm diameter biopsy punch. This confined geometry induced the resultant spheroids to adopt the elongated morphology.

Spheroid Embedding in 3D Collagen I Matrix

Bovine collagen I solution (FibriCol(R), Advanced Biomatrix, 5133) was prepared at a final concentration of 6 mg/mL for spheroid embedding. Briefly, collagen I stock solution was first diluted with de-ionized water containing fluorescent far-red carboxylated polystyrene microparticles (1 μm diameter with 660/690 nm excitation / emission wavelength, Bangs Laboratories, FCFR006). Microparticles were added for a final concentration of 0.05 mg/mL, after being sonicated in a water bath for 30 minutes. The stock solution was adjusted to pH 7.4 using drops of 1N NaOH, which was determined for every batch using a pH meter. Typically, 14–16 μL of 1N NaOH was added per 1 mL of collagen I precursor solution. 4.5% (v/v) of 10$\times$ PBS was added so that the spheroids were not in the hypo-/hyperosmotic condition and prevent salting-out during collagen polymerization. 12.5 mM HEPES was added for buffering effect. The neutralized 7.5 mg/mL collagen solution was then incubated for 1 hour at 4°C and then mixed with MCF-10A growth media containing the hanging drop spheroids. The final mixture were seeded in 96-well plate and incubated at 37°C. After 1 h of incubation, the hydrogel was overlaid with an additional 200 μL of growth media. To apply osmotic pressure on the embedded spheroids, growth media containing 4% wt/vol (100 mOsml^{-}1) polyethylene glycol 400 (TCI Chemicals, N0443) was overlaid. To inhibit matrix metalloproteinase (MMP) activity, growth media contianing 25 μM GM6001 (Millipore Sigma, CC1010) was used. To visualize F-actin structure, the spheroids were treated with 100 nM SiR-actin (Spirochrome, CY-SC001) during hanging drop culture and after embedding in collagen matrix prior to imaging.

Live-cell Confocal Microscopy and Image Processing

Spheroids embedded in the collagen matrix were imaged using Nikon Eclipse Ti fluorescence microscope equipped with a motorized stage, direct illumination LED (Thorburn), a multi-channel light source (Lumencor Spectra-X), spinning disk confocal unit (CrestOptics X-Light V2), cMOS camera (Andor Neo), and a 20$\times$ Plan Apo opjective (NA 0.75). Cells were maintained in a microscope-mounted incubator (In Vivo Scientific) under controlled conditions of 37 °C, 5% CO_2, and humidification. NIS Element software was used for automated image acquisition. MCF-10A-H2B-mCherry, MCF-10A-ER-Snail-1^{6SA}, and far-red fluo-

rescent microparticles were excited and detected at 555/620 nm, 495/535 nm, and 640/670 nm, respectively. Z-stack images were acquired every 15 or 30 minutes, capturing at least 5 slices with a z-step size ranging from 0.9-5 μm. Only spheroids whose z-positions were higher than 100 μm above the plate bottom were included for imaging to avoid undesirable 2D migration along the plate substrate. Both the number of z-slices and the z-step size were optimized to maximize the number of spheroids imaged in a single experiment while ensuring high-content imaging quality. Each channel of the z-stacks was processed using maximum intensity projection in ImageJ. Microparticle images captured with 640/670 nm channel were stabilized using 'Image Stabilizer' plugin, with the option 'Log Transformation Coefficients' option enabled. The transformation log was subsequently applied to the other channels using the 'Image Stabilizer Log Applier' plugin, to ensure consistent stabilization across all the channel images. Spheroid binary masks were generated from the stabilized mCherry signal images dictated with 620 nm channel using a custom ImageJ macro. Briefly, unevenly illuminated background was corrected using 'Substract Background' function with a rolling ball radius of 50 pixels. Median filter with radius of 4.0 px was applied for denoising. 'Smooth' functions was applied, if necessary. The denoised images were binarized with 'Threshold' function. To include the nuclei seprated from the center mass, a 30 pixel-wide band was created using 'Make Band' function, followed by 'Enlarge' with -27 pixels. The completed mask images were saved as image sequences. The stabilized images and mask were later used for kymograph construction and optical flow analysis.

ECM Pore Size Estimation

The fibrillar microstructure of collagen I hydrogel was visualized using confocal reflectance imaging (Leica SP8, 63X, 1.2 N.A. water objective). The pore sizes of ECM were estimated based on our previously established method for fiber counting [53] Firstly, individual fibers were detected with CT-FIRE. Parameters were kept default except for 'thresh_im2' and 's_xlinkbox' to be manually optimized to be 90 and 2 respectively. Subsequently, fiber features were obtained with CurveAlign [54]. Each reflectance image was subdivided into square boxes that are sized 4^2, 8^2, 16^2, 32^2, 64^2, 128^2, 256^2, 512^2, and 1024^2, pixels. The mean number of fibers over all boxes was recorded at various box sizes. A relationship between the box size (box area in μm^2) and number of fibers was established by constructing a cubic interpolant. To estimate fiber density (and the mesh area) in the image, the area corresponding to a single fiber was approximated using the cubic interpolation function. The pore diameter was then calculated by dividing by π, taking the square root and multiplying by 2.

Mechanical Characterization of Gels

An atomic force microscope (MFP-3D-BIO, Asylum Research) in contact mode was used to measure the elastic modulus of collagen I gels. Bovine collagen I (FibriCol, Advanced Matrix) was again prepared at a final concentration of 6 mg/mL and a droplet of 100 μL was dispensed onto a 18×18 mm^{2}sterile glass cover slip (12541014, Fisher Scientific), then transferred to a Petri dish. A spherically tipped cantilever was used with a 5 μm borosilicate beads at the end of silicon nitride, triangular cantilevers (Bruker Corporation, MLCT-O10, $k \sim 0.03$ N/m). The atomic force microscope was calibrated by calculating cantilever spring constants based on the power spectral density of the thermal noise fluctuations. Finally, a 4x4 array of indentation sites in 2 distinct locations on 3 gels were collected with an indentation rate of 10 μm/sec. The resulting force-indentation cures were fit to the Hertz contact model for spherical indentation of a flat surface. A trigger force of 2 nN was used to maintain indentations ranging from 0.5 to 1.5 μm.

Kymograph Analysis

Kymographs were generated using custom MATLAB code. At each time point, the outermost 20 μm thick shell along the perimeter was selected from the binary mask. The selected region was then sliced at 0.5° intervals. Each slice was superimposed onto the corresponding mCherry signal images. The resulting

trapezoid-shaped image slices were interpolated into rectangular shape and then vertically concatenated into a column. The reference angle $\theta = 0°$ was assigned to the angular position of the point farthest from the centroid in the initial image. Each column from successive time points was again horizontally concatenated to construct the final kymograph. For mosaic spheroids, the same procedure was applied to the EGFP channel image, which was then merged with the kymograph generated from the mCherry signal image.

Optical Flow and Coordination Parameter Analysis

The velocity profiles of cellular migration and bead displacement were obtained using Farneback optical flow algorithm. We adapted 'opticalFlowFarneback' function that is available from 'Computer Vision Toolbox' of MATLAB, with default property values. For cellular migration analysis, velocity bias due to the abrupt global movement of the spheroid was calibrated by subtracting the mode value of v_x and v_y. The resulting v_x and v_y were then converted into $v_r = \mathbf{e_r} \cdot (v_x, v_y)$ and $v_\theta = \mathbf{e}_\theta \cdot (v_x, v_y)$ where $\mathbf{e_r} = \frac{(x-x_c, y-y_c)}{r}$ and $\mathbf{e}_\theta = \left(-\frac{y-y_c}{r}, \frac{x-x_c}{r}\right)$, with respect to the centroid of the corresponding binary masks, (x_c, y_c). The peripheral coordination parameter, D was defined to describe the fraction of velocity pixels oriented circumferentially in the outermost region. Outermost 30 μm thick shell along the perimeter was selected as the analysis ROI to sufficiently encompass at least a single cell layer. For each pixel in the ROI, $\text{sgn}(\hat{\mathbf{r}} \times \hat{\mathbf{v}})$ was calculated, where $\hat{\mathbf{r}}$ is a radial unit vector from the spheroid centroid and $\hat{\mathbf{v}}$ is a unit velocity vector. D has a value 0 for a pixel whose velocity is perfectly radially oriented, and 1 or -1 for a pixel whose velocity has a circumferential component. The mean $\langle \text{D} \rangle$ was then calculated across all pixels within the analysis ROI. The orbiting phase was defined as the period during which the $|\langle \text{D} \rangle|$ is greater than 0.5, indicating more than 75% of the cells in the ROI are orbiting in the same direction. After identifying the primary orbiting direction (clockwise or counterclockwise), $\langle \text{D} \rangle$ during the orbiting phase was adjusted to be always positive, to ensure that the orbiting phase is consistently represented as a crest in the plot.

ECM Deformation Analysis

Deformation fields in the surrounding extracellular matrix were analyzed by measuring the displacement of tracers using optical flow, which were verified using manual tracking as well as q-factor-based digital image correlation [55]. Briefly, far-red fluorescent microparticles with 1 μm diameter were embedded in the collagen I matrix and imaged using spinning disk confocal microscopy using z-slices at 5 μm interval. To track the large displacements over time, we determined the positional changes of the initial grid points ($\mathbf{T}_{grid}(t_0)$) by sequentially accumulating the short-term displacements ($\mathbf{u}_{grid}(t)$) between consecutive images (time = $t-1$ and t) captured at 15-20 minutes by adopting the Farneback's bead movement in MATLAB (R2024b, MathWorks, Inc.) The displacement for each updated grid point ($\mathbf{T}_{grid}(t)$) at a given time was obtained by interpolating the optical flow displacement field ($\mathbf{u}_{grid}(t)$) at its corresponding position. Finally, we mapped the cumulative large displacements($\mathbf{C}_{grid}(t)$) on the Cartesian grids by calculating differences between the updated trajectories($\mathbf{T}_{grid}(t)$) and their initial position($\mathbf{T}_{grid}(t_0)$) (Fig. S4 B,C,and D).

$$T_{(\text{i,j})}(t) = T_{(\text{i,j})}(t-1) + u_{(\text{i,j})}(t-1) \tag{1}$$

$$C_{(\text{i,j})}(t) = T_{(\text{i,j})}(t) - T_{(\text{i,j})}(t_0) \tag{2}$$

Displacement Arrays of Rendered Tractions (DART) analysis was performed on the 2D displacement data obtained from optical flow analysis of tracer particles, inspired by our previous work [36]. We constructed a displacement vector field U_{grid}, where U_{grid} is either equal to C_{grid} or u_{grid}, depending on whether DART analysis was performed on the cumulative (C_{grid}) or incremental (u_{grid}) displacement field. The unit radial vector n_{grid}, defined as the vector pointing from the centroid of the spheroid toward each grid poin, was used

to decompose U_{grid} into its radial, U^r_{grid}, and circumferential, U^θ_{grid}, components.

$$U^r_{\text{grid}} = |U_{\text{grid}} \cdot n_{\text{grid}}| \tag{3}$$

$$U^\theta_{\text{grid}} = |U_{\text{grid}} - (U_{\text{grid}} \cdot n_{\text{grid}}) n_{\text{grid}}| \tag{4}$$

Subsequent classification of each displacement vector into protrusive and contractile was determined by the sign of U^r_{grid}. Each particle's position was binned into one of 36 angular regions depending on their location with respect to the center of the spheroid, and their displacement magnitudes classified according to their value. The mean of each displacement type at each angular region was plotted to obtain a radial DART diagram.

$$U^i = \begin{cases} U^{\text{protrusive}} & \text{if } U^r_{\text{grid}} > 0 \\ U^{\text{contractile}} & \text{if } U^r_{\text{grid}} < 0 \end{cases} \tag{5}$$

Statistical Analysis

The number of experimental replications and spheroids represented in all box plots is detailed in each figure caption. The line inside the box indicates the median value while the bottom and the top of the box represent 25th and 75th percentiles, respectively. Error bars denote the minimum and maximum data. To quantify the enhancement of deformation patterns associated with the invasive morphology of spheroids, we measured the amplitude of these patterns over time. This was achieved by calculating the average radial deformation in 36 angular sections around the spheroids. A repeated-measures analysis of variance (ANOVA) was then conducted to evaluate the effect of time on the progression of deformation patterns. Specifically, we compared cumulative deformation changes at three key phases: the pre-orbiting phase (2 hours after seeding), the orbiting phase (12 hours after seeding), and the invading phase (24 hours after seeding). To track changes in temporal displacement magnitude during the orbiting phase, we calculated the 75th percentile of displacement magnitudes around the spheroids, as this metric accounts for the highly localized nature of displacement vectors. The Kruskal-Wallis H test, a non-parametric alternative to one-way ANOVA, was employed to evaluate temporal differences in displacement magnitude. The Bonferroni correction was applied to adjust for multiple comparisons for both analyses. To compare the projected area of spheroids under osmotic compression, two-tailed test was performed at each daily time point. If not specified, all pairwise comparisons were performed using two-tailed t-test, and multi group comparisons were conducted using one-way ANOVA with HSD *post hoc*. All statistical analyses were conducted using SPSS (IBM).

Computational Agent-Based Model

We adapted an existing mathematical model known to produce stable orbiting behavior in the absence of boundaries [33, 35, 39]. We model cells as spherically symmetric self-propulsive (active) particles. Cells also experience drag-like forces which act against the cell velocity and is proportional in magnitude to the cube of its speed. Cells interact with other cells and with the ECM via soft repulsion at short distances and adhesion-based attraction at longer scales. The position of cell i at time t, $\mathbf{x}_i(t)$, and its velocity, $\mathbf{v}_i(t)$, are calculated using Newton's second law. The matrix interface is modeled as static discrete particles, with the position of the kth particle denoted by $\mathbf{y}_k$.

The particular cell-cell and cell-ECM forces that we use are adapted from previous works [40]. In brief, they ensure that cells repel each other along the direction of contact at short distances, but attract each other at larger scales of interest. They are reproduced in detail in the Supplementary Information (SI), along with details of how we determine parameter values for this framework. The two key parameters that we vary to generate the phase diagrams in Fig. 6 are the cell-cell (f_a^{cc}) and cell-matrix adhesion strengths (f_a^{cm}). These parameters are varied from zero to a fraction of a critical maximum force, which depends on the strength of cell-cell repulsion (f_r), with the range of repulsive interactions characterized by a typical cell

diameter $d_r = 15$ μm. The equations of motion are solved with an explicit fourth order Runge-Kutta scheme. Simulations are conducted using the SciPy library in Python. Code to simulate the model is available on Github (see Data Availability). Fifty simulations per parameter regime were used to generate Fig. 6 in the main text (see SI, Mathematical Model for additional details).

Phase Diagrams

We quantify orbiting in numerical simulations using the global coordination parameter (i.e. normalized average angular momentum), $\hat{L}$, defined as:

$$\hat{L} = \frac{1}{N}\left|\sum_{i=1}^{N} \hat{\mathbf{x}}_i \times \hat{\mathbf{v}}_i\right|,$$

where N is the total number of agents and $\hat{\mathbf{x}}_i$ and $\hat{\mathbf{v}}_i$ are the unit position and velocity vectors of cell i, assuming the system's center of mass is at the origin. The global coordination parameter ranges from 0 (no collective coordination) to 1 (perfect orbiting). To construct phase diagrams, we vary cell-cell and cell-matrix adhesion strengths within the interval $[0, 0.5F_c]$, where F_c is the maximum adhesive force. The parameter space is discretized into a 40×40 grid, and fifty simulations are performed for each parameter set. We then average $\hat{L}$ over the last 100 h of each simulation and across all runs. To quantify the time to reach the orbiting state, τ, we fit the global coordination parameter as a function of time, to a sigmoid function with a time scale saturation τ (see SI, Mathematical Model for additional details).

Boundary Perturbations

The mathematical model assumes a circular matrix boundary with uniformly distributed particles. To study the impact of boundary geometry we introduce a fixed and static boundary perturbation of height h_p and width k_p by parametrizing the perturbed boundary as

$$\mathbf{y}(\theta) = R_p(\theta)(\cos\theta, \sin\theta), \quad R_p(\theta) = R + h_p \exp\Big\{-\frac{4R^2(\theta-\pi)^2}{k_p^2}\Big\},$$

with the perturbation centered at $\theta = \pi$. For multiple perturbations the procedure is analogous. We also reparametrize the boundary by arc length to maintain a fixed ECM particle density. To keep a constant cell density, the total number of cells is adjusted according to the total area change induced by the perturbation (see SI, Mathematical Model for additional details).

DATA AVAILABILITY

The experimental data that support the findings are available from the corresponding author upon reasonable request. Source data are provided with this paper. Due to file size, computational results in Figure 6 are available from https://github.com/carlesfalco/Spheroid-Orbiting-Model/tree/main/Data%20Fig%206%20(model).

CODE AVAILABILITY

All code used for the displacement analysis and the associated figures in the main text are available on https://github.com/TaeJeong0127/Displacement_Orbiting.

All code used for computational model and associated figure in the main text are available on https://github.com/carlesfalco/Spheroid-Orbiting-Model.

---

[1] P. Rørth, EMBO reports **13**, 984 (2012).
[2] K. Tanner, H. Mori, R. Mroue, A. Bruni-Cardoso, and M. Bissell, Proc Natl Acad Sci U S A **109**, 1973 (2012).
[3] H. Wang, S. Lacoche, L. Huang, B. Xue, and S. Muthuswamy, Proc Natl Acad Sci U S A **110**, 163 (2013).
[4] A. Chin, K. Worley, P. Ray, G. Kaur, J. Fan, and L. Wan, Proc Natl Acad Sci U S A **115**, 12188 (2018).
[5] T. Fessenden, Y. Beckham, M. Perez-Neut, G. Ramirez-San Juan, A. Chourasia, K. Macleod, P. Oakes, and M. Gardel, J Cell Biol **217**, 1485–1502 (2018).
[6] P. A. Fernández, B. Buchmann, A. Goychuk, L. K. Engelbrecht, M. K. Raich, C. H. Scheel, E. Frey, and A. R. Bausch, Nat Phys **17**, 1130 (2021).
[7] T. Brandstätter, D. Brückner, Y. Han, R. Alert, M. Guo, and C. Broedersz, Nat Commun **14**, 1643 (2023).
[8] L. Lu, T. Guyomar, Q. Vagne, R. Berthoz, A. Torres-Sánchez, M. Lieb, C. Martin-Lemaitre, K. van Unen, A. Honigmann, O. Pertz, D. Riveline, and G. Salbreux, Nat Phys (2024).
[9] S. L. Haigo and D. Bilder, Science **331**, 1071 (2011).
[10] M. Cetera, G. Ramirez-San Juan, P. Oakes, L. Lewellyn, M. Fairchild, G. Tanentzapf, M. Gardel, and S. Horne-Badovinac, Nat Commun **5**, 5511 (2014).
[11] K. Doxzen, S. R. K. Vedula, M. C. Leong, H. Hirata, N. S. Gov, A. J. Kabla, B. Ladoux, and C. T. Lim, Integr Biol **5**, 1026 (2013).
[12] F. J. Segerer, F. Thüroff, A. Piera Alberola, E. Frey, and J. O. Rädler, Phys Rev Lett **114**, 228102 (2015).
[13] S. Jain, V. Cachoux, G. Narayana, S. de Beco, J. D'Alessandro, V. Cellerin, T. Chen, M. Heuzé, P. Marcq, R. Mège, A. Kabla, C. Lim, and B. Ladoux, Nat Phys **16**, 802–809 (2020).
[14] S. Lo Vecchio, O. Pertz, M. Szopos, L. Navoret, and D. Riveline, Nat Phys (2024).
[15] A. Glentis, C. Blanch-Mercader, L. Balasubramaniam, T. Saw, J. d'Alessandro, S. Janel, A. Douanier, B. Delaval, F. Lafont, C. Lim, D. Delacour, J. Prost, W. Xi, and B. Ladoux, Sci Adv **8**, eabn5406 (2022).
[16] L. Kaufman, C. Brangwynne, K. Kasza, E. Filippidi, V. Gordon, T. Deisboeck, and D. Weitz, Biophys J **89**, 635–650 (2005).
[17] K. Wolf, Y. I. Wu, Y. Liu, J. Geiger, E. Tam, C. Overall, M. S. Stack, and P. Friedl, Nat Cell Biol **9**, 893 (2007).
[18] C. Gaggioli, S. Hooper, C. Hidalgo-Carcedo, R. Grosse, J. F. Marshall, K. Harrington, and E. Sahai, Nat Cell Biol **9**, 1392 (2007).
[19] K. Cheung, E. Gabrielson, Z. Werb, and A. Ewald, Cell **155**, 1639–1651 (2013).
[20] S. Carey, A. Starchenko, A. McGregor, and C. Reinhart-King, Clin Exp Metastasis **30**, 615 (2013).
[21] K. S. Kopanska, Y. Alcheikh, R. Staneva, D. Vignjevic, and T. Betz, PloS one **11**, e0156442 (2016).
[22] A. Guzman, V. S. Alemany, Y. Nguyen, C. R. Zhang, and L. J. Kaufman, Biomaterials **115**, 19 (2017).
[23] C. Mark, T. Grundy, P. Strissel, D. Böhringer, N. Grummel, R. Gerum, J. Steinwachs, C. Hack, M. Beckmann, M. Eckstein, R. Strick, G. O'Neill, and B. Fabry, eLife **9**, e51912 (2020).
[24] E. Summerbell, J. Mouw, J. Bell, C. Knippler, B. Pedro, J. Arnst, T. Khatib, R. Commander, B. Barwick, J. Konen, B. Dwivedi, S. Seby, J. Kowalski, P. Vertino, and A. Marcus, Sci Adv **6**, eaaz6197 (2020).
[25] L. Perrin, E. Belova, B. Bayarmagnai, E. Tüzel, and B. Gligorijevic, Comm Biol **5**, 758 (2022).
[26] G. Cai, X. Li, S. Lin, S. Chen, N. Rodgers, K. Koning, D. Bi, and A. Liu, Acta Biomater **179**, 192–206 (2024).
[27] M. Guo, I. Y. Wong, A. S. Moore, O. Medalia, J. Lippincott-Schwartz, D. A. Weitz, and R. D. Goldman, Nature Cell Biology , 1210 (2025).
[28] R. A. Foty and M. S. Steinberg, Int J Dev Biol **48**, 397 (2004).
[29] A. Cerchiari, J. Garbe, N. Jee, M. Todhunter, K. Broaders, D. Peehl, T. Desai, M. LaBarge, M. Thomson, and Z. Gartner, Proc Natl Acad Sci U S A **112**, 2287–2292 (2015).
[30] A. Buttenschön and L. Edelstein-Keshet, PLoS computational biology **16**, e1008411 (2020).
[31] O. Trush, C. Liu, X. Han, Y. Nakai, R. Takayama, H. Murakawa, J. A. Carrillo, H. Takechi, S. Hakeda-Suzuki, T. Suzuki, *et al.*, Journal of Neuroscience **39**, 5861 (2019).
[32] C. Falcó, R. E. Baker, and J. A. Carrillo, SIAM Journal on Applied Mathematics , S17 (2024).
[33] M. R. D'Orsogna, Y.-L. Chuang, A. L. Bertozzi, and L. S. Chayes, Physical Review Letters **96**, 104302 (2006).
[34] Y.-X. Li, R. Lukeman, and L. Edelstein-Keshet, Physica D: Nonlinear Phenomena **237**, 699 (2008).
[35] G. Albi, D. Balague, J. A. Carrillo, and J. von Brecht, SIAM Journal on Applied Mathematics **74**, 794 (2014).
[36] S. E. Leggett, M. Patel, T. M. Valentin, L. Gamboa, A. S. Khoo, E. K. Williams, C. Franck, and I. Y. Wong, Proc. Natl. Acad. Sci. U.S.A. **117**, 5655 (2020).
[37] P. A. Janmey, M. E. McCormick, S. Rammensee, J. L. Leight, P. C. Georges, and F. C. MacKintosh, Nature

Materials **6**, 48 (2007).
[38] I. Y. Wong, S. Javaid, E. A. Wong, S. Perk, D. A. Haber, M. Toner, and D. Irimia, Nature Materials **13**, 1063 (2014).
[39] A. L. Bertozzi, T. Kolokolnikov, H. Sun, D. Uminsky, and J. v. Brecht, Communications in Mathematical Sciences **13**, 955 (2015).
[40] J. A. Carrillo, A. Colombi, and M. Scianna, Journal of Theoretical Biology **445**, 75 (2018).
[41] G. Cheng, J. Tse, R. K. Jain, and L. L. Munn, PLoS One **4**, e4632 (2009).
[42] K. L. Mills, R. Kemkemer, S. Rudraraju, and K. Garikipati, PLoS One **9**, e103245 (2014).
[43] W. Tang, A. Das, A. F. Pegoraro, Y. L. Han, J. Huang, D. A. Roberts, H. Yang, J. J. Fredberg, D. N. Kotton, D. Bi, and M. Guo, Nature Physics **18**, 1371 (2022).
[44] E. Boghaert, J. P. Gleghorn, K. Lee, N. Gjorevski, D. C. Radisky, and C. M. Nelson, Proceedings of the National Academy of Sciences **109**, 19632 (2012).
[45] M. Yu *et al.*, Science **339**, 580 (2013).
[46] T. Wittmann, A. Dema, and J. van Haren, Current Opinion in Cell Biology **66**, 1 (2020).
[47] C. Di Ciano-Oliveira, A. C. P. Thirone, K. Szászi, and A. Kapus, Acta Physiologica **187**, 257 (2006).
[48] N. A. Araújo, L. M. Janssen, T. Barois, G. Boffetta, I. Cohen, A. Corbetta, O. Dauchot, M. Dijkstra, W. M. Durham, A. Dussutour, *et al.*, Soft Matter **19**, 1695 (2023).
[49] W. D. Martinson, R. McLennan, J. M. Teddy, M. C. McKinney, L. A. Davidson, R. E. Baker, H. M. Byrne, P. M. Kulesa, and P. K. Maini, eLife **12**, e83792 (2023).
[50] C. S. Dias, M. Trivedi, G. Volpe, N. A. Araújo, and G. Volpe, Nature Communications **14**, 7324 (2023).
[51] E. Tsingos, B. H. Bakker, K. A. Keijzer, H. J. Hupkes, and R. M. Merks, Biophysical Journal **122**, 2609 (2023).
[52] J.-F. Joanny and J. O. Indekeu, Physica A: Statistical Mechanics and its Applications **631**, 129314 (2023).
[53] A. S. Khoo, T. M. Valentin, S. E. Leggett, D. Bhaskar, E. M. Bye, S. Benmelech, B. C. Ip, and I. Y. Wong, ACS biomaterials science & engineering **5**, 4341 (2019).
[54] Y. Liu, A. Keikhosravi, G. S. Mehta, C. R. Drifka, and K. W. Eliceiri, Fibrosis: methods and protocols , 429 (2017).
[55] A. Landauer, M. Patel, D. Henann, and C. Franck, Experimental Mechanics **58**, 815 (2018).

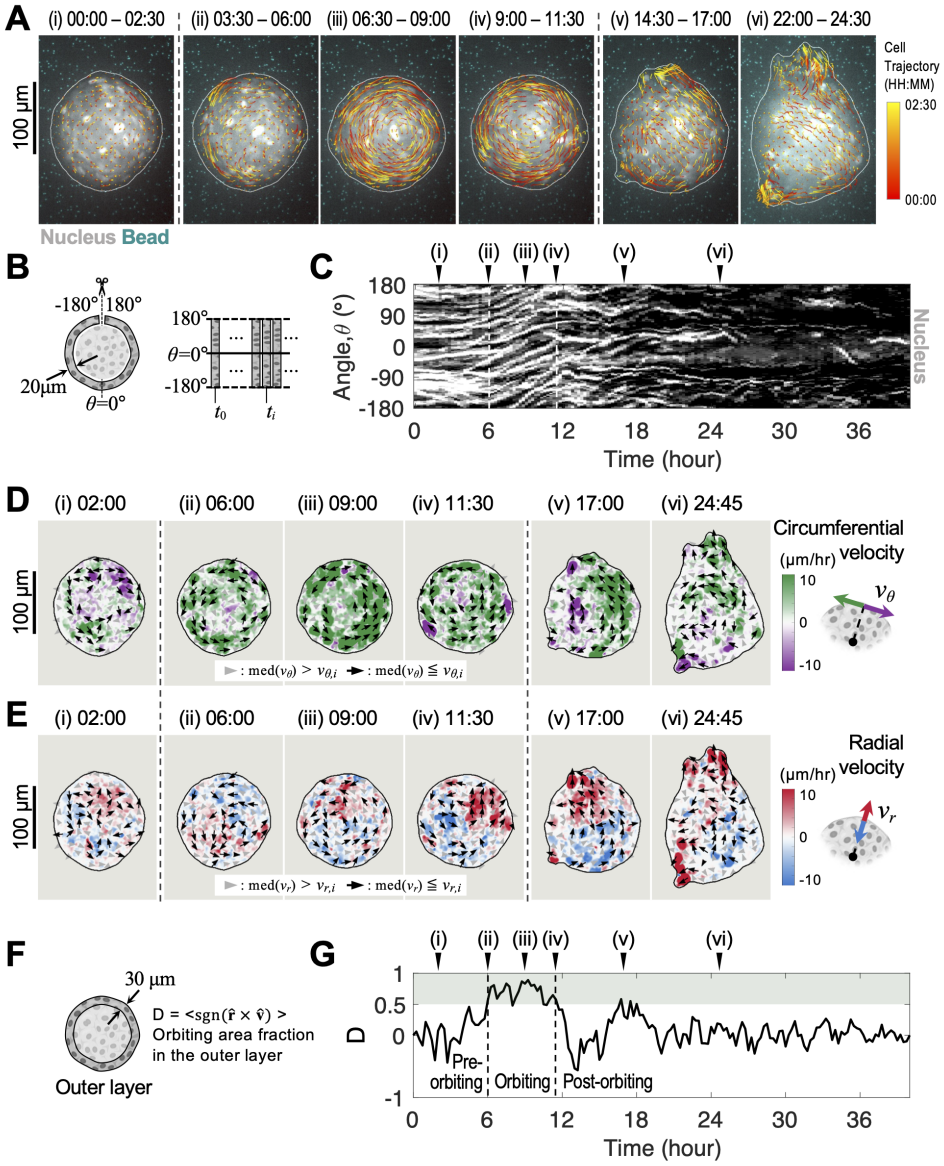

FIG. 1. **Multicellular spheroids transition from circumferential orbiting to radial invasion in 3D matrix.** (**A**) Representative images of the MCF-10A spheroid embedded in a 3D collagen matrix, overlaid with motion fields based on optical flow. (**B**) Schematic of unwrapping and concatenating the outermost 20 μm peripheral "layer" of the spheroid equatorial plane at each time to generate a kymograph. (**C**) Kymograph of fluorescent nuclei (H2B-mCherry) in the outermost peripheral layer of cells shows minimal angular motion from 0-6 h after embedding (i-ii). Next, all nuclei exhibit coordinated angular motion from 6-12 h, indicated by the parallel upward trajectories (iii-iv). Finally, nuclei exhibit minimal and uncoordinated angular motion as they transitioned into radial migration mode (v-vi). (**D**) Circumferential velocity profiles of the spheroid. The magnitude of the angular velocity is color coded from purple to green. Black arrows denote large velocities greater that the median, while gray arrowheads denote smaller velocities less than the median. (**E**) Radial velocity profiles of the spheroid. The magnitude of the radial velocity is color coded from blue to red. Black arrows again denote large velocities greater that the median, while gray arrowheads denote smaller velocities less than the median. (**F**) Peripheral coordination parameter D is based on the fraction of circumferentially migrating cells in the outermost 30 μm peripheral "layer" of the spheroid equatorial plane at each time. (**G**) D $>$ 0.5 from 6-12 h during coordinated orbiting, but is below this value before and after.

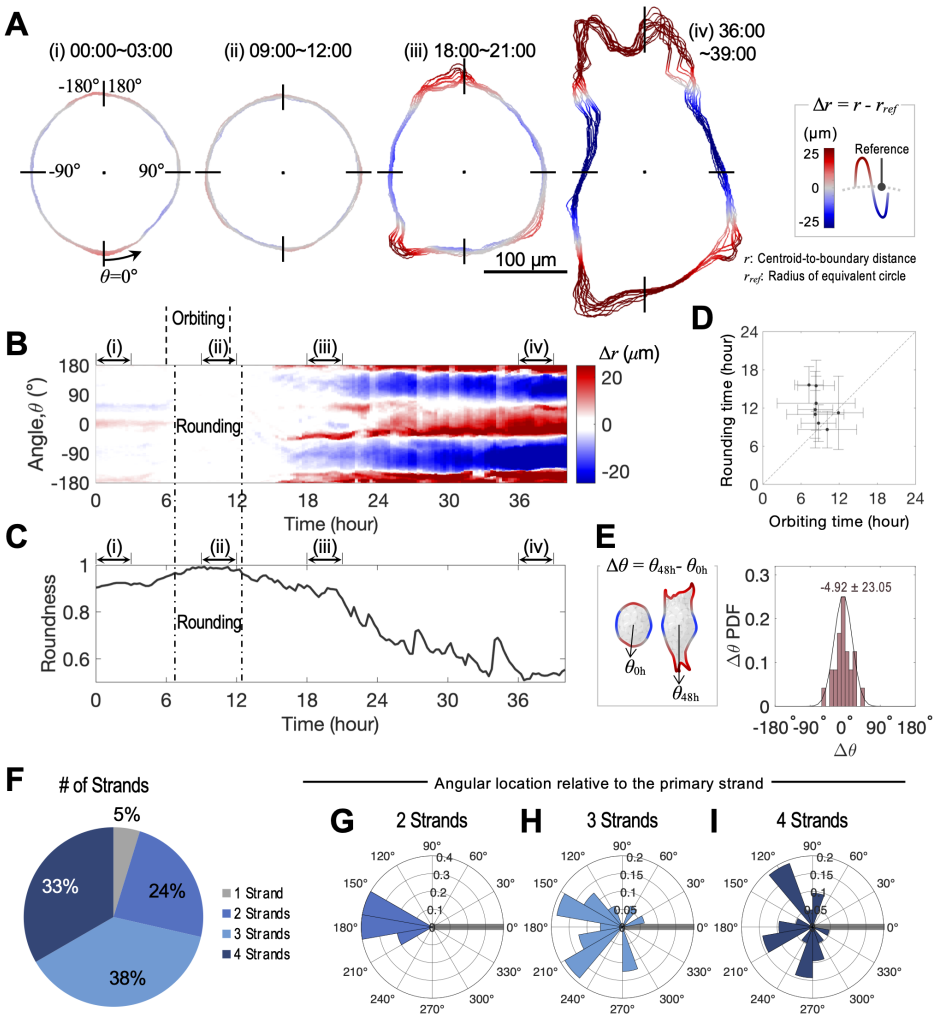

FIG. 2. **Spheroid morphology is initially elongated, rounding up during orbiting, then elongating again along the same axis for strand invasion.** **(A)** Representative spheroid morphology based on cross-section at equatorial axis. The boundary is color-coded by larger (red) or smaller (blue) radial deviation from a reference radius for a perfect circle (gray). The reference radius (r_{ref}) is the radius of equivalent circle, defined as a circle that has the same area and centroid as the spheroid cross-section at each time point. During phase (ii) 09:00∼12:00, the boundary color is mostly gray, indicating that the spheroidal morphologies are comparable to the equivalent circles. **(B)** Kymograph of radial deviation (Δr) along the periphery($-180^\circ - +180^\circ$), highlighting regions of protrusion and flattening at each time. **(C)** Roundness profile during the observation. Increase in roundness value from 6-12 h and decrease thereafter are comparable to orbiting and invasion. **(D)** Comparison of rounding time and orbiting time shows orbiting slightly precedes rounding. The horizontal error bars mark the start and end of the orbiting time, and the vertical error bars mark the start and end of the rounding time. The black dots at their intersections indicate the midpoint of each interval. $n_{\text{spheroids}} = 8$ across duplication. **(E)** Angular difference between the local maxima of Δr at the initial (00:00) and final (48:00) time points. $n_{\text{spheroids}} = 21$ across triplication. **(F-I)** Number and angular distribution of multicellular strands. $\theta = 0^\circ$ (solid gray lines) were set to the angular location of the primary (longest) strand. $n_{\text{spheroids}} = 21$ across 3 biological replicates.

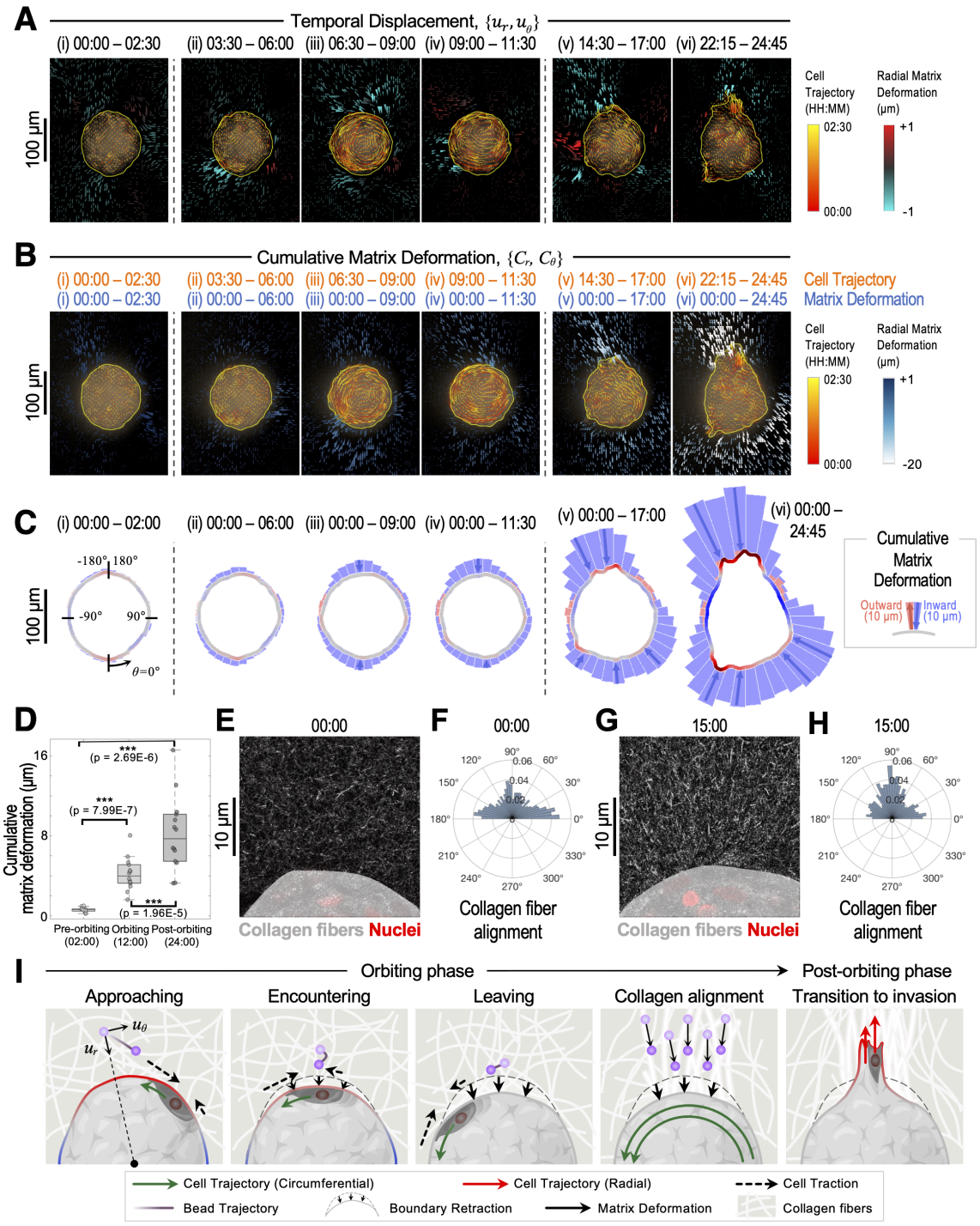

FIG. 3. **Spheroids exert non-uniform deformations on the surrounding matrix, with hotspots along the initial elongation axis**. **(A)** Representative snapshots of a spheroid overlaid with motion fields of cell nuclei and temporal displacement fields of tracer particles (i: Pre-orbiting, ii-iv: Orbiting, v,vi: Invading). **(B)** Representative snapshots of a spheroid, overlaid with motion fields of cell nuclei and cumulative deformation fields of tracer particles at different stages of cell migration. **(C)** DART visualization of inward/outward cumulative particle displacement at various binned angular positions. **(D)** Comparison of cumulative bead displacements based on phase in multiple samples (n = 3, spheroids = 14). The displacement was quantified using the amplitude of undulation patterns in radial displacement along angular coordinates. Repeated-measures ANOVA was conducted for the statistical analysis. Pairwise comparisons were conducted using two-sided paired t-test with Bonferroni correction (Box-plot elements: center line,median; box limits, interquantile range(IQR), Whiskers: 1.5× IQR, *p<0.05, **p<0.01, ***p<0.001). **(E, F)** Confocal reflectance imaging of collagen fibers and their orientation distribution immediately after embedding (00:00). **(G, H)** Confocal reflectance imaging of aligned collagen fibers and their orientation distribution after orbiting phase (15:00). **(I)** Schematic illustrations of two mechanisms of matrix alignment during the orbiting phase. Tractions exerted by orbiting cells remodel the matrix in radial directions due to the sharp curvature near the initial poles; Spheroid-matrix interface retracts as the spheroids round-compact during the orbiting phase.

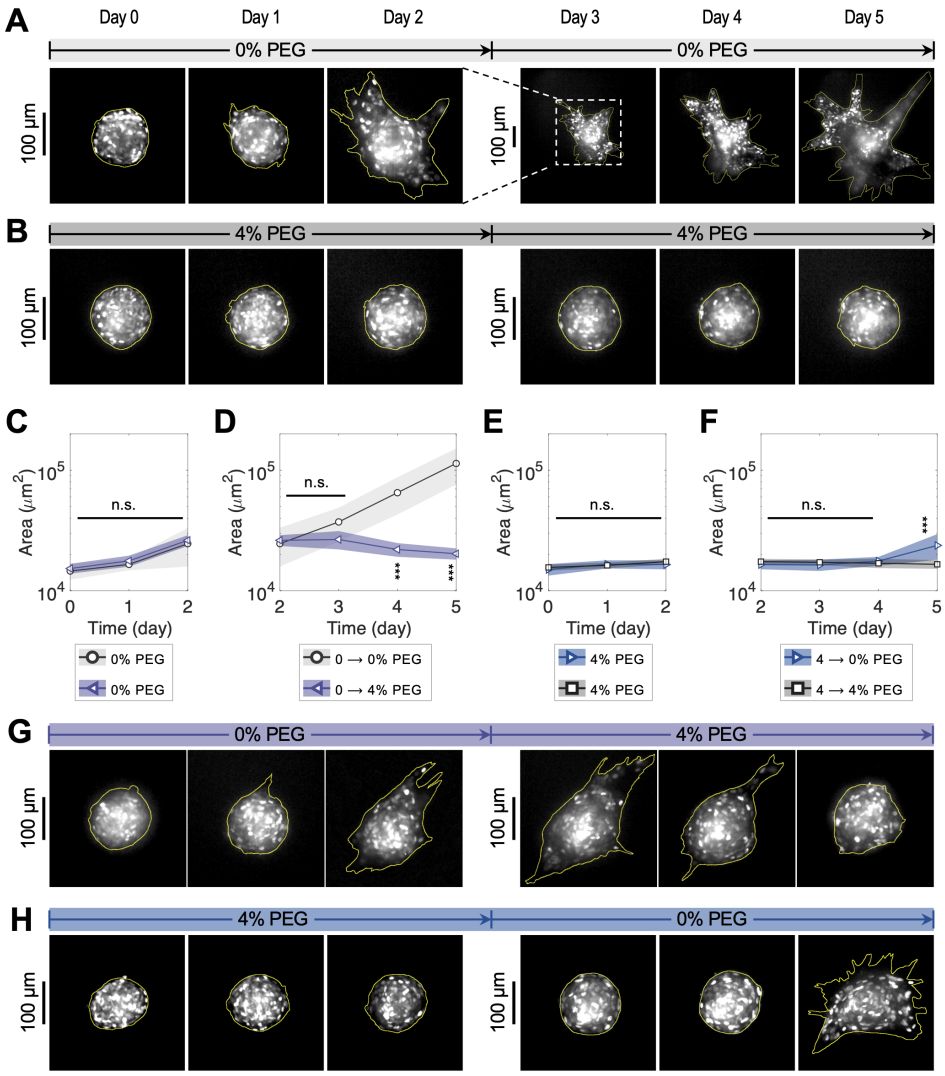

FIG. 4. **Osmotic compression can transiently arrest collective orbiting or reverse matrix invasion**. **(A)** Representative snapshots of coordinated orbiting and invasion over 5 days in normal isotonic media. **(B)** Spheroids are arrested over 5 days in hypertonic media (4% PEG400). **(C, D)** Projected area of the spheroids under each condition. For the first 2 days, spheroids were maintained in 0% PEG media. Afterwards, selected spheroids were transferred to media with 4% PEG media. $n_{0\%\to 0\%} = 5$, $n_{0\%\to 4\%} = 11$, across triplication. Two-tailed Mann Whitney U test ($p < 0.05$:*, $p < 0.01$:**, $p < 0.001$:***). p = 0.377, 0.180, 0.115, 0.069, <0.001, and <0.001 for day 0-5. **(E, F)** Spheroids were maintained in 4% PEG media. Afterwards, selected spheroids were transferred to media with 0% PEG media. $n_{4\%\to 0\%} = 10$, and $n_{4\%\to 4\%} = 7$, across triplication. Two-tailed Mann Whitney U test ($p < 0.05$:*, $p < 0.01$:**, $p < 0.001$:***). p = 0.270, 0.669, 0.109, 0.315, 0.475, and <0.001 for day 0-5. For all plots in (C-F), solid lines with marker points indicate the average value across spheroids, and the shaded area indicates the standard deviation. **(G)** Spheroids initially orbit and invade for 2 days in isotonic media, but then invasion is reversed for the next 3 days in hypertonic media (4% PEG400). **(H)** Spheroids are arrested over 2 days in hypertonic media (4% PEG400), then orbit and invade over the next 3 days in isotonic media.

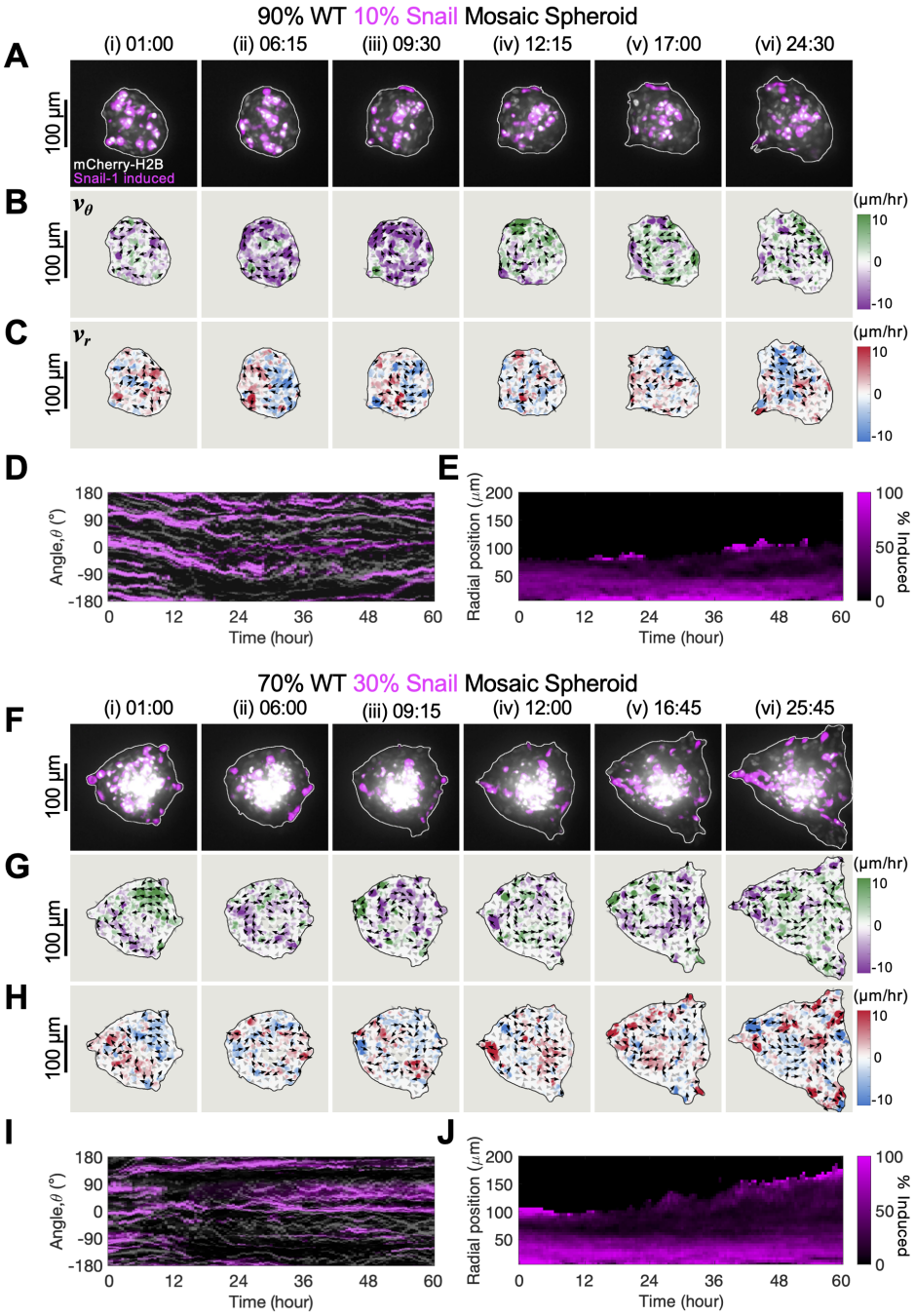

FIG. 5. **Coordinated migration is impeded by increasing fractions of Snail-induced cells (pink) mixed with wild type (WT) cells in mosaic spheroids**. **(A)** Representative snapshots of 10% Snail and 90% WT cells in mosaic spheroids. **(B, C)** spheroids exhibit unimpeded circumferential velocities and hotspots of radial velocity corresponding to matrix invasion. **(D)** Kymograph shows coordinated orbiting of both Snail and WT cells from 0-24 h. **(E)** Snail cells are sorted both the interior and periphery of the spheroid. **(F)** Representative snapshots of 30% Snail and 70% WT cells in mosaic spheroids. **(G, H)** spheroids exhibit weakened circumferential velocities but hotspots of radial velocity corresponding to matrix invasion. **(I)** Kymograph shows no coordinated orbiting of both Snail and WT cells from 0-24 h. **(J)** Snail cells are again sorted both the interior and periphery of the spheroid.

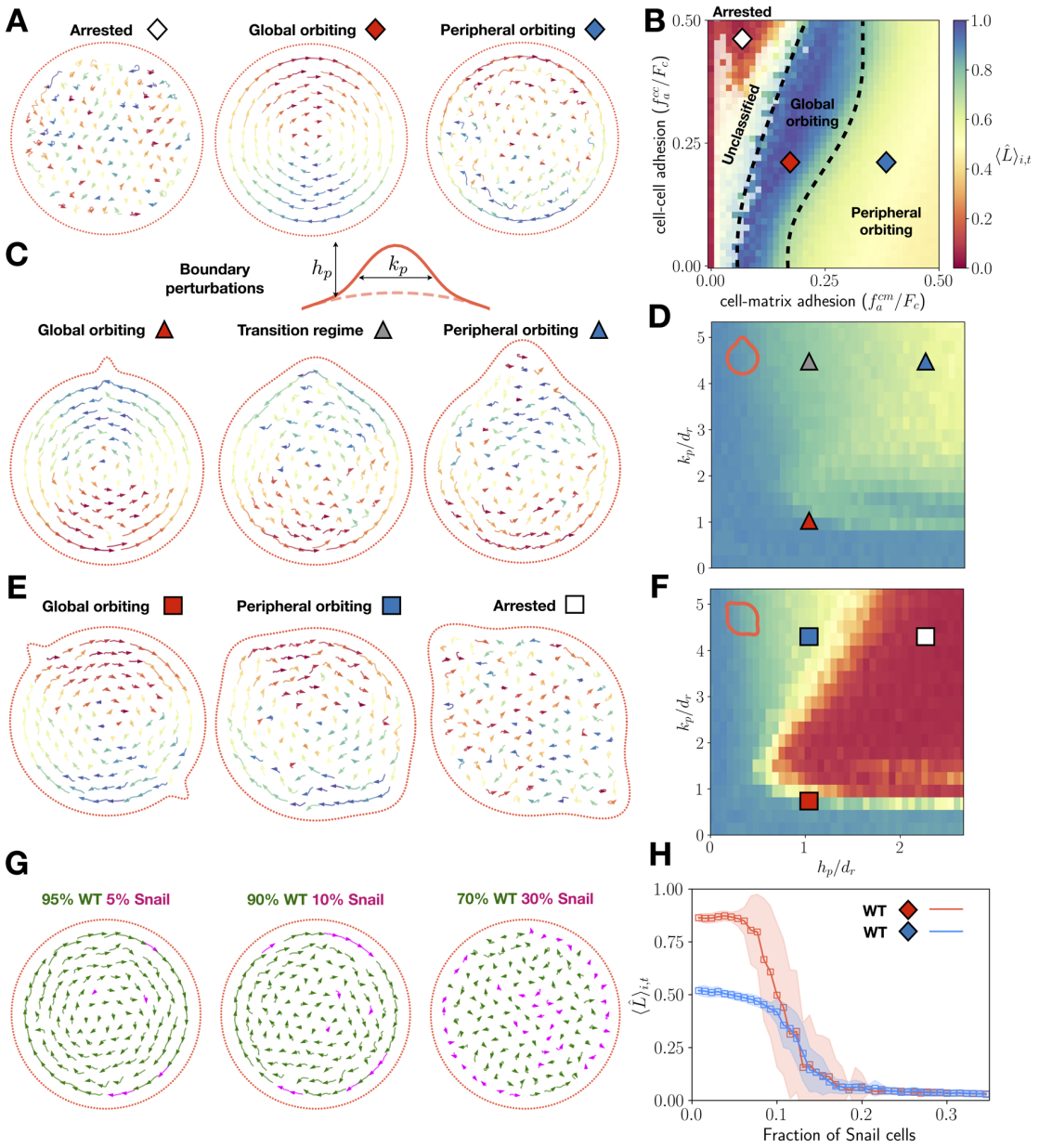

FIG. 6. **Self-propelled particle model elucidates crosstalk of cell-cell and cell-matrix adhesion with boundary geometry**. **(A, B)** Representative simulations of uncoordinated (white diamond), global orbiting (red diamond) and peripheral orbiting (blue diamond) states, and the corresponding phase diagram of the global coordination parameter $\langle L \rangle$ over the last 100 hours of the simulation across various cell-cell and cell-matrix adhesion strength parameters. The dashed lines on the phase diagram are hand-drawn and approximate the boundaries of the three states. Adhesive parameters (f_a^{cc}/F_c, f_a^{cm}/F_c), from left to right, correspond to $(0.05, 0.45)$, $(0.2, 0.2)$, and $(0.2, 0.4)$. **(C, D)** Representative snapshots of global (red triangle), transitory (grey triangle) and peripheral orbiting (blue triangle) associated with a single boundary perturbation, and the corresponding phase diagram of the global coordination parameter across varying perturbation heights (h_p) and widths (k_p). Parameters h_p and k_p are variables incorporated into the Boundary Perturbation model defined in Materials and Methods section. Orbiting is generally maintained with a single boundary perturbation, regardless of its width and height, since particles can follow a relatively large continuous section of curved boundary. Boundary perturbation parameters, $(h_p/d_r, k_p/d_r)$, from left to right, given by $(1, 1)$, $(1, 4)$, and $(2.4, 4)$. **(E, F)** Representative snapshots of global orbiting (red square), peripheral orbiting (blue square) and uncoordinated migration (white square) with two oppositely-oriented boundary perturbations, and the corresponding phase diagram depicting how the global coordination parameter phase diagram responds to different perturbation heights and widths. Global orbiting transitions towards uncoordinated motility with two boundary perturbations of increasing width and height, due to cells sensing smaller continuous section of curved boundary. Boundary perturbation parameters, from left to right, given by $(1, 1)$, $(1, 4)$, and $(2.4, 4)$. **(G, H)** Snapshots of simulations with increasing percentages of Snail+ cells, which are assumed to have lower cell-cell adhesion and higher cell-matrix attraction compared to WT cells. The corresponding phase plot of the global coordination parameter as a function of Snail percentage demonstrates how global orbiting is disrupted by increasing fractions of Snail cells, which sort to the boundary and impede collective migration. Red indicates global orbiting and blue indicates peripheral orbiting, corresponding to (A). Shaded regions denote plus or minus one standard deviation from the mean.

Supplementary Information

Collective transitions from orbiting to matrix invasion in 3D multicellular spheroids

Jiwon Kim[1], Hyeontae Jeong[1], Carles Falcó[2], Alex M. Hruska[1], W. Duncan Martinson[3], Alejandro Marzoratti[1], Mauricio Araiza[4], Haiqian Yang[5], Vera C. Fonseca [6], Stephen A. Adam[7], Christian Franck[3], José A. Carrillo[2], Ming Guo[5], and Ian Y. Wong[1]

[1]School of Engineering, Legoretta Cancer Center, Brown University, 184 Hope St Box D, Providence RI 02912, USA

[2]Mathematical Institute, University of Oxford, Oxford, OX2 6GG, United Kingdom

[3]The Francis Crick Institute, 1 Midland Road, London, NW1 1AT, United Kingdom

[4]Department of Mechanical Engineering, University of Wisconsin-Madison, 11513 Engineering Dr, Madison, WI 53706, USA

[5]Department of Mechanical Engineering, Massachusetts Institute of Technology, 77 Massachusetts Avenue, Cambridge, Massachusetts 02139, USA

[6]Department of Pathology & Laboratory Medicine, Brown University. Box G-B377, Providence RI 02912, USA

[6]Department of Cell and Developmental Biology, Northwestern University. 320 E. Superior Street. Chicago, IL 60611, USA

Contents

1 Mathematical model

1.1 Model description. We model cells as discrete particles moving off-lattice in a 2D domain. Our decision to use a 2D model is motivated by the observation that cell movement between different layers of the spheroids appears to be limited, however we note that the framework described below can be extended naturally to 3D. Cells are treated as active particles subject to drag (frictional) forces. We incorporate two key terms to describe these dynamics: a self-propulsion term proportional to the velocity of cell i, and a nonlinear drag (friction) term which acts against the cell velocity and is proportional in magnitude to the cube of the cell speed. This formulation, commonly used in models of self-propelled particles as a first approximation for active movement [1, 2, 4], naturally predicts an equilibrium speed at which cells travel where friction balances self-propulsion such that the speed of cell i is given by $|\mathbf{v}_i| = \sqrt{\alpha/\beta} =: u$ in the absence of other forces.

We assume that cells can interact with each other and with their ECM boundary via cell-cell, $\mathbf{F}^{cm}$, and cell-matrix, $\mathbf{F}^{cm}$, forces which each encode soft repulsion at short distances and adhesion-based attraction at longer distances. The strength and magnitude of the cell-cell (*resp.* cell-matrix) force is assumed to depend on the relative displacement between the cell and its neighbor (*resp.* neighboring ECM molecule). The cell-matrix force additionally depends on the direction in which the cell travels, as we will later introduce the assumption that cells can only adhere to ECM molecules within a specified angle of this direction. The specific functions that yield the cell-cell and cell-ECM forces are described in more detail in the ensuing paragraphs.

We model the ECM boundary as a set of discrete equally spaced particles to simplify numerical calculations of cell-matrix forces and facilitate the introduction of boundary perturbations. This modeling approach further admits straightforward interpretation of how specific ECM molecules affect cell movement. For a circular boundary of radius R made up of M points, the position of the l^{th} ECM molecule is given by $\mathbf{y}_l = (R\cos(2\pi l/M), R\sin(2\pi l/M))$ for $l = 1, \ldots, M$. In the main text of this manuscript, we assume that these points are static so that we may focus on how the boundary geometry, cell-cell, and cell-matrix force influence the stability of collective orbiting in a controlled setting.

We use Newton's second law to supply ordinary differential equations (ODEs) dictating how the position and velocity of cell i, $\mathbf{x}_i(t)$ and $\mathbf{v}_i$, respectively, change over time $t \geq 0$ in response to the active, drag, cell-cell, and cell-matrix forces. The system of ODEs is given

by

$$\frac{\mathrm{d}\mathbf{x}_i}{\mathrm{d}t} = \mathbf{v}_i\,, \tag{1}$$

$$\frac{\mathrm{d}\mathbf{v}_i}{\mathrm{d}t} = \underbrace{\left(\alpha - \beta|\mathbf{v}_i|^2\right)\mathbf{v}_i}_{\text{active and drag forces}} + \underbrace{\sum_{j\neq i,\, j=1}^{N} \mathbf{F}^{cc}(\mathbf{x}_j - \mathbf{x}_i)}_{\text{cell-cell repulsion/attraction}} + \underbrace{\sum_{k=1}^{M} \mathbf{F}^{cm}(\mathbf{y}_k - \mathbf{x}_i, \mathbf{v}_i)}_{\text{cell-ECM repulsion/attraction}}\,, \tag{2}$$

$$\frac{\mathrm{d}\mathbf{y}_k}{\mathrm{d}t} = \mathbf{0}\,, \tag{3}$$

where $\mathbf{y}_l$ denotes the position of the l^{th} ECM molecule. We have slightly abused notation by absorbing the mass of the cell into the terms on the right-hand side of Eqs. (1)-(2).

We consider the direction of cell-cell and cell-matrix forces to be aligned with the displacement vector, $\mathbf{r}$, between a cell and its neighboring cell or ECM molecule. The magnitudes of both forces are further assumed to only depend on the distance between these two objects. This is captured by using two radially symmetric kernels, $K^{cc}(|\mathbf{r}|)$ and $K^{cm}(|\mathbf{r}|)$, which are related to the forces via

$$\mathbf{F}^{cc}(\mathbf{r}) = K^{cc}(|\mathbf{r}|)\frac{\mathbf{r}}{|\mathbf{r}|}, \tag{4}$$

$$\mathbf{F}^{cm}(\mathbf{r}, \mathbf{v}) = \tilde{H}(|\mathbf{r}|,\, \hat{\mathbf{r}}\cdot\hat{\mathbf{v}} - \cos\theta_{\max})\, K^{cm}(|\mathbf{r}|)\frac{\mathbf{r}}{|\mathbf{r}|}\,. \tag{5}$$

The term which is unique to the cell-ECM force, $\tilde{H}(\cdot,\cdot)$, is a modified Heaviside function that arises from an assumption that cells can only adhere to matrix molecules that fall within an angle $\theta_{\max} \in [0, \pi]$ of their unit velocity vector $\hat{\mathbf{v}}$. Repulsive forces are not assumed to be affected by the modified Heaviside function, as they are assumed steric in origin and therefore isotropic. The assumption of anisotropic cell-ECM adhesion accelerates the emergence of collective orbiting, but we show in Fig. A8 that orbiting is robust across a large array of values for $\theta_{\max}$. The modified Heaviside function is defined as

$$\tilde{H}(r,\, \lambda) = \begin{cases} 1, & \text{if } 0 < r < d_r; \\ H(\lambda), & \text{if } r \geq d_r\,; \end{cases}$$

where $H(\cdot)$ is the standard Heaviside function.

In all numerical simulations, we fix the angular sensing region such that the cells do not adhere to ECM molecules which lie outside an angle $\theta_{\max} = \pi/3$ from its current velocity

vector. In Fig. A8 we quantify the impact of this parameter, showing that results are robust under similar values. Note also that cell-matrix adhesion changes the equilibrium velocity of cells, such that the long-term cell speed will be slightly larger than $u = \alpha/\beta$.

For simplicity we assume that repulsion (f_r) is identical for cell-cell and cell-matrix interactions, while adhesion depends on two parameters, f_a^{cc} and f_a^{cm}, that correspond to the respective kernel. While there are multiple possibilities for the functional forms of the repulsive and attractive kernels, for example power-law or exponentially decaying functions [1, 4], we opt instead to use kernels which ensure that cells do not experience forces from objects which lie beyond a certain maximum distance. The cell-cell and cell-matrix kernels used in this manuscript are based on [3], which have compact support and have been well characterized. They are given by

$$K^{\ell}(r) = \begin{cases} -f_r \left(\dfrac{d_r}{2r}\right)^{3-2s}, & \text{if } 0 < r < \frac{d_r}{2}; \\ \dfrac{2f_r(r-d_r)}{d_r}, & \text{if } \frac{d_r}{2} \leq r < d_r; \\ -\dfrac{4f_a^{\ell}(r-d_a)(r-d_r)}{(d_a-d_r)^2}, & \text{if } d_r \leq r < d_a; \\ 0, & \text{if } r \geq d_a, \end{cases} \tag{6}$$

where $\ell \in \{cc, cm\}$, $s \in (0, 2]$ is a parameter that captures the behavior of the kernel near the origin and is related to the cell nucleus stiffness, d_r is a typical cell diameter, and d_a gives the range of adhesive interactions. For the simulations in the main text, we set $s = 1.25$, which corresponds to a singular kernel at the origin. In the sections below, we show that a different choice of the exponent s affects the results only qualitatively. This is consistent with previous work using the same family of kernels [3]. Fig. A1 shows a plot of this kernel.

1.2 H-stability and adhesion parameter ranges. We use the concept of H-stability from statistical mechanics to constrain the range of admissible model parameters [3]. This constraint ensures that cells do not "collapse" to a single point as more individuals are added to the simulation. In biological terms, this means that there is a sufficient balance between repulsive and attractive forces such that, as more individuals are added into a simulation space, cells do not form clusters with a distance less than a cell diameter. If the kernels are not H-stable, then unphysical solutions can arise in which a very large number of particles occupies a small, finite region of space.

Mathematically, a kernel or potential is H-stable if the total potential energy of the system is

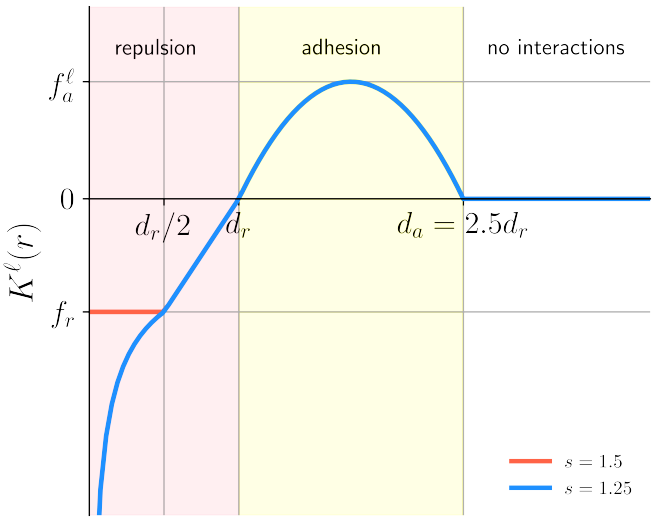

Figure A1: Representation of the interaction kernels $K^\ell(r)$. Parameters are not to scale.

bounded below by a constant that is independent of the number of particles. This concept has been applied in the context of interacting models of cell migration and is well-characterized for the kernel in Eq. (6) [3]. (This is another motivating reason for why we have used the kernels described abov). In particular, given an interaction potential $u_\ell(r)$, such that $K^\ell(r) = u'_\ell(r)$, K^ℓ is called H-stable if

$$\int_0^{+\infty} u_\ell(r) r \, \mathrm{d}r > 0 \, .$$

If the integral is negative, then the kernel is not H-stable (also called "catastrophic"). For the kernel in Eq. (6), the integral above yields the following constraint on the strength of repulsive and attractive forces:

$$\frac{f_r}{f_a^\ell} > \frac{32s(d_a - d_r)(3d_a^2 + 4d_a d_r + 3d_r^2)}{5(11s+6)d_r^3} := F_* \, . \tag{7}$$

Following these ideas, in numerical simulations we vary the cell-cell and cell-matrix adhesion strengths in $f_a^\ell \in [0, F_c]$, with $F_c := f_r/F_*$ so that the potential is always H-stable.

To illustrate the impact of H-stability, we present snapshots of numerical simulations in which the kernels are not H-stable — see Fig. A2. Depending on the H-stability of the cell-cell and cell-matrix interactions, the system either collapses to the center of the spheroid or to its boundary.

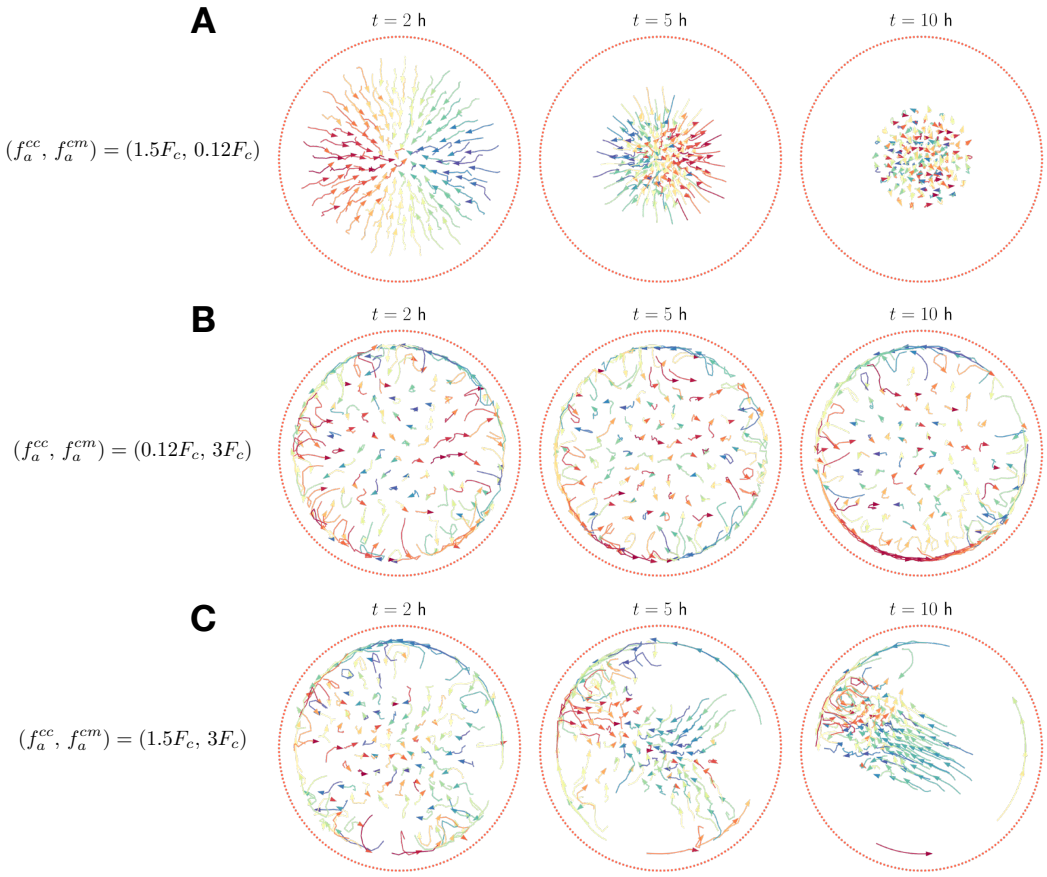

Figure A2: Interaction kernels that are not H-stable lead to cell collapse and unphysical behavior. Snapshots of numerical simulations where: (A) K^{cc} is not H-stable; (B) K^{cm} is not H-stable; and (C) neither is H-stable.

1.3 Model parameters. We set the radius of the circular ECM boundary, $R = 100$ μm, to have a comparable length scale to experimentally observed spheroid radii. For simplicity, the length scales of repulsive and adhesive forces, d_r and d_a, and the strength of repulsive forces f_r, are assumed to be identical for cell-cell and cell-matrix interactions. The parameter d_r can be estimated from cell-cell spacing observed in experiments, while d_a can be similarly estimated by noting that MCF-10A cells do not appear to interact with neighbors beyond $2-3$ cell diameters. This leads us to fix $d_r = 15$ μm, $d_a = 2.5d_r = 37.5$ μm. The experimental data also provide sufficient information to fix the asymptotic cell speed, which is roughly equal to $u = \sqrt{\alpha/\beta} = 3$ μm/h. The average cell velocity in numerical simulations, however, is higher than u —around 10 μm/h— due to the additional tangential acceleration provided by cell-matrix adhesion. Furthermore, we note that fixing the cell speed determines the ratio of the parameters α and β but not their specific values.

The number of discrete ECM particles, M, is chosen to be sufficiently large to avoid cell escape from the spheroid, yet also small enough to ensure that the net cell-matrix force on a given cell is no more than an order of magnitude larger than the cell-cell repulsion force. We have found that, for the parameters used in this manuscript, $M = 200$ molecules is sufficient to achieve both goals. For a circular ECM boundary of radius $R = 100$ μm, this corresponds to a one-dimensional ECM density of 0.32 molecules/μm, which is approximately five times larger than the one-dimensional density corresponding to the external layer of orbiting cells.

The number of cells, N, is similarly chosen to maximize the number of individuals in the spheroid while simultaneously limiting the degree of overlap between them, as otherwise repulsive forces overly dominate cell movement and uncoordinated behavior occurs. Since cells are assumed to be spherically symmetric, the problem reduces to finding the maximum number of identical circles that fit within a unit circle without overlapping. Although this classical problem only has explicit solutions for relatively small numbers [5], we note that the density of known solutions appears to asymptotically approach a value of $0.75 - 0.85$ circles/units^2 as the number of circles increases. For circles of radius $d_r/2 = 7.5$ μm embedded in a larger circle of radius $R = 100$ μm, about $130 - 140$ circles are needed to achieve a comparable density. Consequently, we set $N = 130$ cells for the simulations.

We have thus far fixed all but four parameters in the mathematical model, with α, f_r, f_a^{cc}, and f_a^{cm} remaining undetermined. The adhesion-related parameter values are constrained by Eqn. (7), ensuring that the cell-cell and cell-matrix potentials are H-stable. As it is unclear what are reasonable values for these parameters, we sweep over various values in the main text to determine how they influence the long-term system behavior. Meanwhile, the parameter f_r sets the timescale to reach the equilibrium orbiting scale. All simulations in the main text have $f_r = 100$ μm/h^2 as we observe in numerical simulations that this corresponds to an equilibrium timescale of around $10-20$ h. Finally, α^{-1} represents the timescale at which cells readjust their velocities as a consequence of active and drag forces. To prevent cells from escaping the spheroid, the acceleration caused by cell-matrix repulsion must dominate over the acceleration arising from active-drag forces, which drives changes in the velocity $\Delta v \sim u$ during timescales approximately equal to α^{-1}. Consequently, the condition $f_r \gg u\alpha$ is fulfilled, and we set $\alpha = 0.01, 0.1, 1\,\text{h}^{-1}$, all of which satisfy this requirement.

We summarize in Table 1 the model parameters and their chosen values. We also study in the next sections the impact of varying different model parameters.

Table 1: Summary of model and simulation parameters and their values used in numerical simulations.

Parameter	Values	Units	Meaning
α	10^{-2}, 10^{-1} (main text), 10^{0}	h^{-1}	self-propulsion coefficient
u	3	μm/h	equilibrium cell speed in the absence of cell-cell and cell-matrix forces
β	α/u^2	$\mathrm{h}/\mu\mathrm{m}^2$	friction coefficient
d_r	15	μm	repulsion interaction range
d_a	$2.5d_r$	μm	adhesion interaction range
f_r	100 (main text)	$\mu\mathrm{m}/\mathrm{h}^2$	cell-cell and cell-matrix repulsion strength
F_c	5.18 (main text)	$\mu\mathrm{m}/\mathrm{h}^2$	critical adhesion strength for H-stability (Eq. (7))
f_a^{cc}	$[0, 0.5F_c]$ (main text), $1.5F_c$ (Fig. A2)	$\mu\mathrm{m}/\mathrm{h}^2$	cell-cell adhesion strength
f_a^{cm}	$[0, 0.5F_c]$ (main text), $3F_c$ (Fig. A2)	$\mu\mathrm{m}/\mathrm{h}^2$	cell-matrix adhesion strength
$\theta_{\max}$	$\pi/3$ (main text), $[0, \pi]$ (Fig. A8)	rad	maximum cell-matrix alignment angle (Eq. (5))
s	1.25	—	exponent controlling the repulsive force behavior at the origin
ρ	0.004	cells/$\mu\mathrm{m}^2$	cell density
N	130 (circular boundary) $+ n_p\rho\Delta A$ (boundary perturbations, Eq. (13))	cells	number of cells
M	200	molecules	number of ECM molecules
R	100	μm	spheroid radius
h_p	$[0, 40]$	μm	height of boundary perturbation
k_p	$[0, 80]$	μm	width of boundary perturbation
n_p	$1, 2, 3$	—	number of boundary perturbations

1.4 Numerical implementation. We solve the system of ODEs given by Eqns. (1)-(3) in Python, using an explicit fourth order Runge-Kutta scheme with time step $\Delta t = 0.1$h. Initial cell positions were sampled uniformly at random within a circle of radius $R = 100$ μm and with a minimum interparticle distance of 10 μm. Initial velocities were similarly sampled uniformly at random, with each component of the velocity sampled uniformly on the interval $[-\sqrt{10}, \sqrt{10}]$ μm/h.

1.5 Curvature, matrix detection angle, and orbiting. Here we derive a minimal geometric condition relating the spheroid radius R, the repulsive interaction range d_r, the adhesive range d_a, and the maximum matrix-detection angle $\theta_{\max}$ that must be satisfied for a cell to attach to the matrix molecules when the boundary is curved. In this calculation we assume that the density of matrix molecules is sufficiently high so that cell-matrix attachment can occur. We also assume that $\theta_{\max} < \pi/2$, as otherwise attachment can always occur given that $d_a > d_r$.

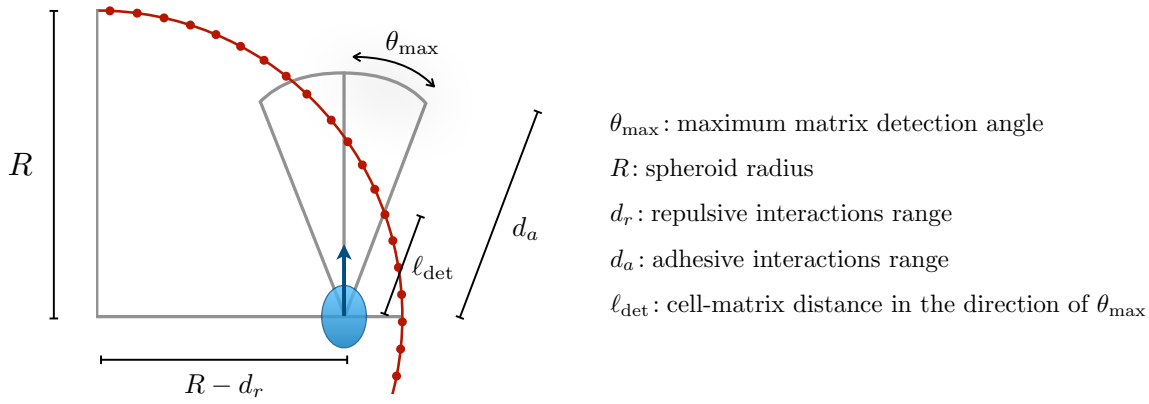

Figure A3: Schematic of the spheroid boundary (circle of radius R) and a cell (blue dot) located a distance d_r inside the boundary (i.e. at radial coordinate $R - d_r$). A detection ray (gray lines) is cast at angle $\theta_{\max}$. Its intersection with the spheroid defines the cell–matrix distance ℓ_{det}, which must lie within the adhesive interaction range d_a for successful attachment. Distances are only schematic and are not representative of the values chosen for the mathematical model.

Basic trigonometry gives the intersection distance, ℓ_{det} by solving

$$|(R - d_r, 0) + \lambda(\sin\theta_{\max}, \cos\theta_{\max})| = R,$$

which leads to a quadratic equation for λ. Taking the positive solution yields

$$\frac{\ell_{\mathrm{det}}}{d_r} = \left(\frac{R}{d_r} - 1\right) \sin\theta_{\mathrm{max}} \left[-1 + \sqrt{1 + \frac{(2R/d_r - 1)}{(R/d_r - 1)^2 \sin^2\theta_{\mathrm{max}}}}\right].$$

Requiring $\ell_{\mathrm{det}} < d_a$ gives the attachment condition

$$\left(\frac{R}{d_r} - 1\right) \sin\theta_{\mathrm{max}} \left[-1 + \sqrt{1 + \frac{(2R/d_r - 1)}{(R/d_r - 1)^2 \sin^2\theta_{\mathrm{max}}}}\right] < \frac{d_a}{d_r}. \tag{8}$$

The flat boundary limit can be obtained for $R \gg d_r$, by expanding the square root to first order in d_r/R, and the criterion $\ell_{\mathrm{det}} < d_a$ simplifies to

$$\frac{d_r}{d_a} < \sin\theta_{\mathrm{max}},$$

which is the straight boundary detection condition.

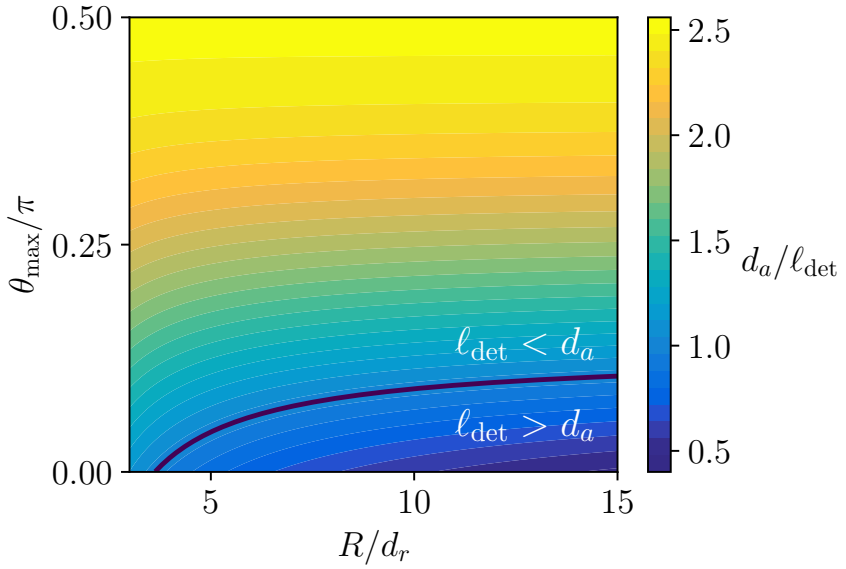

Figure A4: Attachment diagram for $d_a/d_r = 2.5$. Higher values of d_a/ℓ_{det} correspond to a larger portion of the boundary that cells can detect. The solid black curve marks the equality in Eq. (8), separating regions where attachment is or is not possible.

For $d_a/d_r = 2.5$, the attachment relationship is satisfied over a large region of the $(R/d_r, \theta_{\mathrm{max}})$ parameter space, as illustrated in Figure A4. In particular, a smaller spheroid radius —

and thus a larger curvature — and wider detection angles facilitate successful cell–matrix attachment. While further analytical progress seems challenging, we provide further evidence of the role of curvature by using spheroids of a varying aspect ratio in Section 5.4

2 Angular momentum

We quantify orbiting with using the normalized average angular momentum, $\hat{L}$, as an order parameter. Its value is defined as

$$\hat{L} = \frac{1}{N}\left|\sum_{i=1}^{N} \hat{\mathbf{x}}_i \times \hat{\mathbf{v}}_i\right| , \tag{9}$$

where $\hat{\mathbf{x}}_i$ denotes the unit position vector of cell i and $\hat{\mathbf{v}}_i$ its unit velocity vector. Note that, with this definition, we have assumed the system center of mass is located at the origin. This order parameter satisfies $\hat{L} \geq 0$ and also

$$\hat{L} \leq \frac{1}{N}\sum_{i=0}^{N} |\hat{\mathbf{x}}_i \times \hat{\mathbf{v}}_i| \leq 1 .$$

with equality when each position vector is orthogonal to its corresponding velocity vector. Notably, this occurs in a perfectly coordinated state where all cells orbit either clockwise or anticlockwise. Hence, values of the angular momentum close to unity indicate global orbiting. By contrast, order parameter values close to zero are indicative that most cells do not exhibit collective coordination.

In all model analyses we use the full normalized angular momentum, computed over all tracked cells. This choice is essential as it allows us to clearly separate uncoordinated motion, peripheral orbiting, and global orbiting, whereas restricting the metric to cells within 30 μm of the boundary produces similarly high values for peripheral and global orbiting, making them indistinguishable (Fig. A5).

2.1 Phase diagrams. To produce the phase diagrams in the main text, we vary the strengths of cell-cell and cell-matrix adhesion, f_a^{cc} and f_a^{cm}, respectively, within the interval $[0, 0.5F_c]$, as predicted by the H-stability analysis. These values are chosen because, for strong cell-cell adhesion ($f_a^{cc} > 0.5F_c$), we observed parameter combinations that do not provide sufficient coverage of the spheroid. The parameter space $[0, 0.5F_c] \times [0, 0.5F_c]$ is discretized into a 40×40 grid, and fifty simulations corresponding to 300 h are performed for each

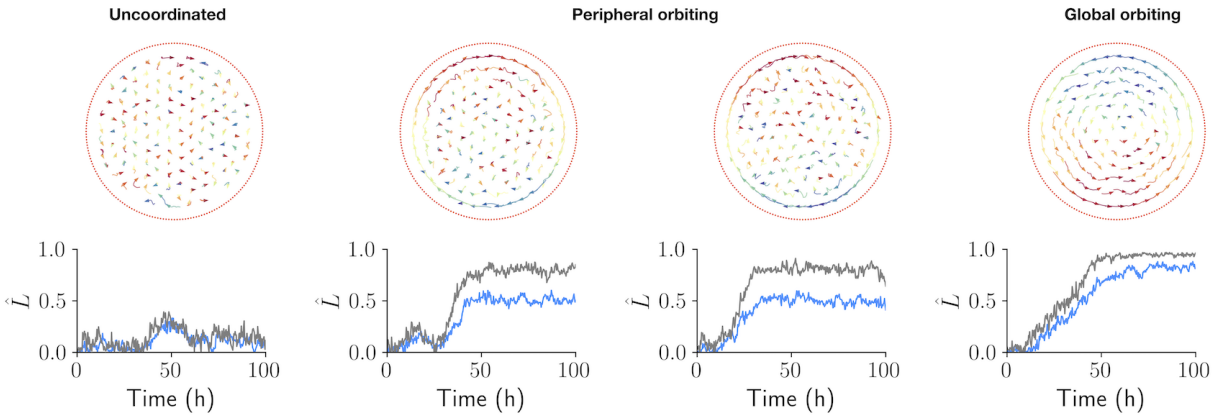

Figure A5: Normalized angular momentum separates orbiting modes. (top) Representative cell trajectories. (bottom) Time courses of the normalized angular momentum corresponding to each numerical simulation. The blue curve uses all tracked cells; the gray curve uses only cells within 30 μm of the boundary.

parameter combination. All other parameters are kept fixed, and numerical simulations differ only in their initial conditions. We then average the normalized angular momentum over the last 100 h of the numerical simulation and across the fifty different simulations. We denote by $\langle\cdot\rangle_i$ averages with respect to the simulation replicates, and by $\langle\cdot\rangle_t$ the averages with respect to time.

Numerically, we observe that cell-matrix interactions drive the emergence of collective orbiting within the first few hours of the simulation. In contrast, when cell-matrix adhesion is weak, collective orbiting does not appear within the first $\sim 100-200$ h. However, in a small fraction of simulations, global orbiting eventually emerges over much longer timescales. In these cases, the average normalized angular momentum, $\langle\hat{L}\rangle_{i,t}$, takes up to $\sim 10^3$ h to reach equilibrium. Here, collective orbiting arises purely due to geometric boundary constraints, as cell-matrix adhesion is almost negligible, leading to a significantly longer coordination timescale. To identify such cases, we check whether the increase in normalized angular momentum during the last 100 h is greater than 0.1 — corresponding to a slope of more than 0.001 in a linear regression fit. Simulations meeting this criterion are labeled as *unclassified* and appear white in the phase diagram.

2.2 Timescale to reach orbiting. To quantify the time to reach the orbiting state, τ, we first average $\hat{L}$ across the simulation replicates to obtain $\langle\hat{L}\rangle_i$. We then fit $\langle L\rangle_i$ as a function of time, to a sigmoid function using non-linear least squares. The sigmoid function,

defined as

$$\hat{L}(t) = L_0 + \frac{L_{\text{eq}}}{1 + \exp\left(-(t-\tau)/b\right)}, \tag{10}$$

depends on time, t, and on four parameters: the initial angular momentum, L_0; the equilibrium angular momentum, L_{eq}; the time at which $\hat{L} = L_0 + L_{\text{eq}}/2$, τ; and a parameter that quantifies the steepness of the sigmoid, b. The fitted parameter (τ) is shown in Fig. A9, along with representative snapshots of numerical simulations and their corresponding average angular momentum dynamics.

2.3 Scaling with number of orbiting layers. In experiments and numerical simulations we often observe states in which only cells within the external layers of the spheroid orbit, while cells near the center remain uncoordinated. To quantify this, we study how the angular momentum scales with the number or orbiting layers, n_{orb}. Given the typical distance between cells, a, and the outer radius of the spheroid, R, n_{orb} is a non-negative integer between 0 and R/a. Next, we observe that the number of orbiting cells in a layer of radius r_j is approximately $2\pi r_j/a$, where the allowed values for r_j are given by $r_j = R - ja$, with $j = 1, \ldots, n_{\text{orb}}$. By assuming that uncoordinated cells negligibly influence the total angular momentum of the system and all cells within orbiting layers are perfectly aligned, we can approximate Eq. (9) as

$$\hat{L} \approx \frac{2\pi}{N} \frac{(R-a) + (R-2a) + \ldots + (R - n_{\text{orb}}a)}{a} = \frac{2\pi n_{\text{orb}}}{N} \left(\frac{R}{a} - \frac{n_{\text{orb}} + 1}{2} \right). \tag{11}$$

When the maximum number of possible layers $n_{\text{orb}} = R/a \gg 1$, this approximation further reduces to

$$\hat{L} \approx \frac{2\pi R}{Na} \left(\frac{R}{2a} - \frac{1}{2} \right) \approx \frac{\pi R^2}{Na^2} = 1\,,$$

so it is consistent with the expected angular momentum value for a global orbiting state.

Identifying the typical distance between cells as $a \sim \rho^{-1/2} = R\sqrt{\pi/N}$, Eq. (11) becomes independent of the geometry of the spheroid

$$\hat{L} \approx \frac{2\pi n_{\text{orb}}}{N} \left(\sqrt{\frac{N}{\pi}} - \frac{n_{\text{orb}} + 1}{2} \right). \tag{12}$$

In particular, for our numerical simulations with $N = 130$, the normalized angular momentum should correspond to $\hat{L} \sim 0.26, 0.48, 0.64, 0.76$ for one, two, three, and four layers, respectively. We use this criterion to generate a discretized version of the phase diagram

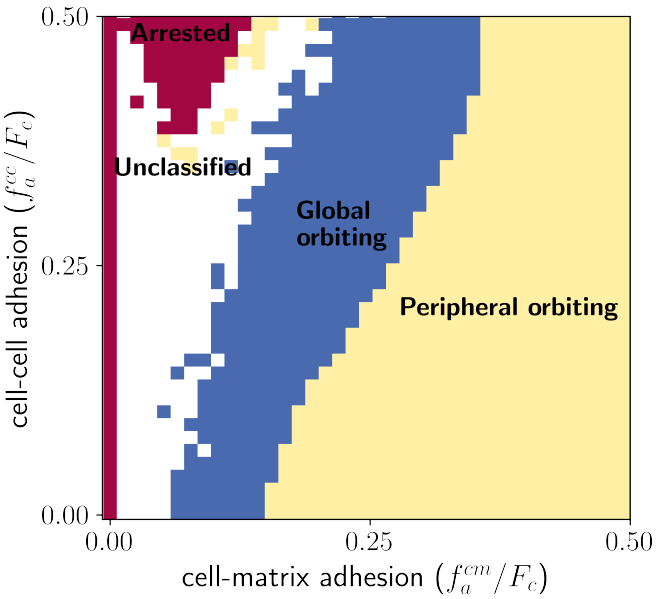

Figure A6: The mathematical model predicts three regimes based on collective orbiting behavior. States are classified according to the number of orbiting layers, as determined by the normalized angular momentum: arrested ($\langle \hat{L} \rangle_{i,t} < 0.24$, no layers), global orbiting ($0.24 \leq \langle \hat{L} \rangle_{i,t} < 0.76$, one to three layers), and peripheral orbiting ($\langle \hat{L} \rangle_{i,t} \geq 0.76$, four or more layers). Unclassified states reach equilibrium only after very long times.

in the main text (Fig. 6B), classifying states into four categories based on whether $\langle L \rangle_i$ reaches equilibrium within 200 h and the approximate number of orbiting layers (see Fig. A6). States labeled as arrested do not exhibit orbiting within 300 h of simulation but may transition to an orbiting state over much longer timescales.

3 Boundary perturbations

All numerical simulations in the previous sections used a circular matrix boundary, given by the position of discrete particles $\mathbf{y}_l = (R\cos(2\pi l/M), R\sin(2\pi l/M))$ for $l = 1, \ldots, M$. Here, we introduce boundary perturbations with height h_p, and width k_p. The perturbed circle can be parametrized by $\theta \in [0, 2\pi]$, with the peak of the perturbation found at $\theta = \pi$:

$$\mathbf{y}(\theta) = R_p(\theta)\,(\cos\theta,\, \sin\theta)\,, \quad R_p(\theta) = R + h_p \exp\{-4R^2(\theta-\pi)^2/k_p^2\}\,.$$

The case of boundary perturbations at n_p different locations can be considered analogously. In numerical simulations, we reparametrize the perturbed boundary by the arc length pa-

rameter to generate matrix particles with a fixed density ($200/2\pi R \approx 0.32$ cells/μm).

3.1 Change of area due to perturbation. To keep constant cell density inside the spheroid, we calculate the change in area due to one boundary perturbation

$$\begin{aligned}\Delta A &= \frac{1}{2}\int_0^{2\pi} R_p(\theta)^2\,\mathrm{d}\theta - \pi R^2 \\ &= Rr_p\int_0^{2\pi} e^{-4R^2(\theta-\pi)^2/k_p^2}\,\mathrm{d}\theta + \frac{r_p^2}{2}\int_0^{2\pi} e^{-8R^2(\theta-\pi)^2/k_p^2}\,\mathrm{d}\theta \\ &\approx \sqrt{\pi}r_p\frac{k_p}{2} + \sqrt{\pi}r_p^2\frac{k_p}{4\sqrt{2}R} = \sqrt{\pi}r_p\frac{k_p}{2}\left(1+\frac{r_p}{2\sqrt{2}R}\right). \end{aligned} \tag{13}$$

Numerical simulations consider a number of cells given by $N = \rho(\pi R^2 + n_p\Delta A)$.

3.2 Main text model parameters. To produce the figures in the main text (Fig. 6), we vary boundary perturbation parameters on the ranges $0 \le h_p \le 40\,\mu$m, $0 \le k_p \le 80\,\mu$m. We average the angular momentum over the last 100 h of the simulation. Since the model parameters are fixed, but we study orbiting stability for a varying ECM geometry, we extend the final simulation time to 500 h. After this time, all simulations appear to have converged to equilibrium. We choose adhesive parameters corresponding to the global orbiting regime $(f_a^{cc}, f_a^{lm}) = (0.2F_c, 0.2F_c)$. The rest of model parameters are taken as explained in Section 1 — see also Table 1.

3.3 Matrix forces at the onset of invasion. As a first approximation to study the transition from coordinated orbiting to radial invasion, we visualize the forces applied on the matrix molecules that arise solely from the adhesive component of the cell–matrix interaction (Fig. A7). These simulations provide a mechanistic counterpart to the experimental observations by isolating how boundary geometry redistributes cell–matrix forces and, in turn, collective motion. With a perfectly circular boundary, the model yields globally coordinated orbiting with reaction forces that are predominantly tangential and only weakly radial — consistent with tracer displacements that decompose into circumferential and inward components. Introducing a single local perturbation to the boundary geometry focuses adhesive reaction forces that point more strongly inward at the perturbation, biasing cells to migrate along the periphery near that site and initiating the transition from global to peripheral orbiting. Adding a second perturbation further fragments the tangential guidance, ampli-

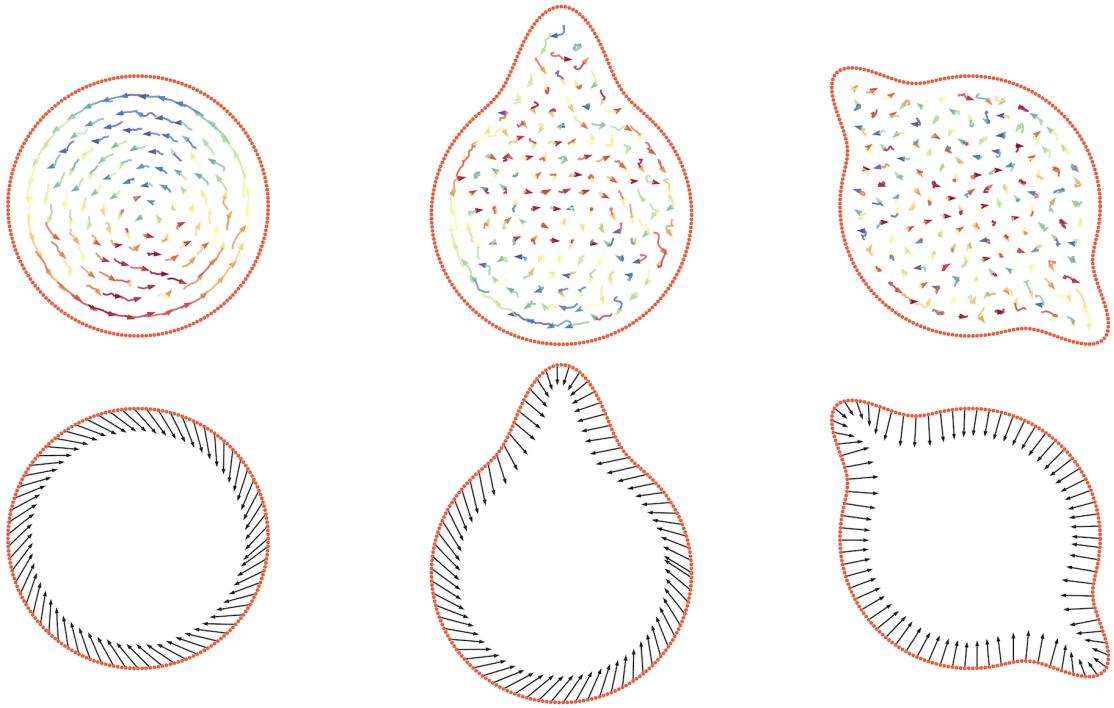

Figure A7: Snapshots of three simulations with different matrix boundaries: left, perfect circle (global orbiting); middle, one matrix perturbation (transition to peripheral orbiting); right, two perturbations (loss of coherence and uncoordinated motion). Bottom row shows forces experienced by matrix molecules due to the adhesive component of the cell–matrix interaction (black arrows along the boundary). The directions and relative magnitudes of these forces indicate a promoted invasive tendency at the onset of the orbiting instability. Arrow lengths encode relative strength only and are not absolute magnitudes.

fies competing inward pulls, and breaks coordination — consistent with the experimentally observed loss of coherent orbiting.

4 Mosaic spheroids

4.1 Model description and parameters. To describe the mosaic spheroid experiments, we consider a version of the mathematical model with two cell species. Both wildtype (WT)

(1) and Snail cells (2) follow the same equations, but with different model parameters,

$$
\begin{aligned}
\frac{\mathrm{d}\mathbf{x}_i^{(1)}}{\mathrm{d}t} &= \mathbf{v}_i^{(1)}\,,\\
\frac{\mathrm{d}\mathbf{v}_i^{(1)}}{\mathrm{d}t} &= \left(\alpha - \beta\left|\mathbf{v}_i^{(1)}\right|^2\right)\mathbf{v}_i^{(1)} + \sum_{l\neq i,\, j=1}^{N_1} \mathbf{F}_{11}^{cc}(\mathbf{x}_l^{(1)} - \mathbf{x}_i^{(1)}) + \sum_{l=1}^{N_2} \mathbf{F}_{12}^{cc}(\mathbf{x}_l^{(2)} - \mathbf{x}_i^{(1)}) + \sum_{k=1}^{M} \mathbf{F}_1^{cm}(\mathbf{y}_k - \mathbf{x}_i^{(1)}, \mathbf{v}_i^{(1)})\,,\\
\frac{\mathrm{d}\mathbf{x}_j^{(2)}}{\mathrm{d}t} &= \mathbf{v}_j^{(2)}\,,\\
\frac{\mathrm{d}\mathbf{v}_j^{(2)}}{\mathrm{d}t} &= \left(\alpha - \beta\left|\mathbf{v}_j^{(2)}\right|^2\right)\mathbf{v}_j^{(2)} + \sum_{l=1}^{N_1} \mathbf{F}_{21}^{cc}(\mathbf{x}_l^{(1)} - \mathbf{x}_j^{(2)}) + \sum_{l\neq j,\, l=1}^{N_2} \mathbf{F}_{22}^{cc}(\mathbf{x}_l^{(2)} - \mathbf{x}_j^{(2)}) + \sum_{k=1}^{M} \mathbf{F}_2^{cm}(\mathbf{y}_k - \mathbf{x}_i^{(2)}, \mathbf{v}_i^{(2)})\,,\\
\frac{\mathrm{d}\mathbf{y}_k}{\mathrm{d}t} &= \mathbf{0}\,,
\end{aligned}
$$

where N_1 and N_2 are the number of WT and Snail cells respectively; $\mathbf{F}_{11}^{cc}$, $\mathbf{F}_{22}^{cc}$ represent adhesive-repulsive forces between the same type of cell; and $\mathbf{F}_{21}^{cc}$, $\mathbf{F}_{12}^{cc}$ represent cross-interaction forces.

Table 2: Summary of two-species model and simulation parameters and their values used in numerical simulations. The remaining model parameters (cell-cell repulsion, active-drag forces, and ECM geometry) are the same as in the one-species case (Table 1).

Parameter	Values	Units	Meaning
N_1	$\{85, 86, \ldots, 130\}$	cells	number of WT cells
N_2	$N - N_1$	cells	number of Snail cells
$f_{a_{1,1}}^{cc}$	$0.2F_c$	μm/h^2	cell-cell adhesion strength (WT-WT)
$f_{a_{1,2}}^{cc}$, $f_{a_{2,1}}^{cc}$	0	μm/h^2	cell-cell adhesion strength (WT-Snail)
$f_{a_{2,2}}^{cc}$	0	μm/h^2	cell-cell adhesion strength (Snail-Snail)
$f_{a_1}^{cm}$	$0.2F_c$, $0.4F_c$	μm/h^2	cell-matrix adhesion strength (WT-ECM)
$f_{a_2}^{cm}$	$0.8F_c$	μm/h^2	cell-matrix adhesion strength (Snail-ECM)
$\theta_{\max}^{(1)}$	$\pi/3$	rad	maximum cell-matrix alignment angle (WT)
$\theta_{\max}^{(2)}$	π (main text), $\pi/3$ (Fig. A14)	rad	maximum cell-matrix alignment angle (Snail)

The forces, $\mathbf{F}_1^{cm}$ and $\mathbf{F}_2^{cm}$, model cell-matrix interactions for each cell type, similarly to the one-species case. These forces follow the expressions in Eqs. (4)-(6). We also note that active and drag forces are identical for both cell types. We summarize the chosen model parameters to produce Fig. 6 in the main text in Table 2. As in the previous section, we solve numerically the model until a final time of 500 h, and record angular momentum using the last 100 h of the simulation. Cells are initialized as in the one-species case.

5 Additional simulations

In this section, we present additional numerical simulations of the model, where we test the impact of varying different model parameters.

5.1 Cell-matrix alignment angle ($\theta_{\max}$). We begin by exploring the impact of the cell-matrix alignment angle $\theta_{\max}$(see Fig. A8), which sets the maximum angle between the cell velocity and the relative position to the spheroid boundary (Eq. (5)). As expected intuitively, we find that for small values of $\theta_{\max}$, orbiting is disrupted easily. The angular momentum parameter peaks at a value close to 1 (for comparable cell-cell and cell-matrix adhesion parameters), and for values close to those used in the main text ($\theta_{\max} = \pi/3$). Numerical results remain consistent with the main text for larger values of the maximum cell-matrix alignment angle ($\theta_{\max} \sim 0.3\pi - 0.8\pi$). Interestingly, when $\theta_{\max}$ is close to π, meaning that cells can adhere to the matrix from nearly any direction except directly behind them, global orbiting appears to be more stable. This may be due to the increased range over which cells can detect and interact with the matrix, enhancing their ability to align with the boundary. However, in the limit of isotropic interactions, orbiting is completely disrupted ($\langle \hat{L} \rangle_{i,t} \sim 0$), highlighting the crucial role of anisotropy in cell-matrix interactions for the emergence of orbiting.

5.2 Active-drag forces (α, β). The main text uses a self-propulsion parameter of $\alpha = 0.1$ h^{-1}, setting a timescale for speed readjustments due to active-drag forces at approximately 10 hours. This choice yields realistic cell speeds. To explore the effect of this parameter on orbiting behavior (Fig. A9), we vary α by an order of magnitude ($\alpha = 10^{-2}$, 10^{0} h^{-1}) while adjusting the friction coefficient, β, to keep the equilibrium speed in the absence of cell-matrix interactions, $\sqrt{\alpha/\beta} = u$, constant.

In both cases, the phase diagram reveals regions of global orbiting, peripheral orbiting, and arrested motion (Fig. A9). The timescales to reach these states remain largely unchanged, supporting our numerical findings that they are primarily governed by the strength of the interaction kernel. Additionally, Fig. A9 suggests that cell speeds decrease with increasing self-propulsion strength, consistent with the equilibrium speed being determined by the balance between active-drag and cell-matrix forces.

While all three cases exhibit similar behavior, when $\alpha = 10^{-2}$ h^{-1}, a larger portion of the phase diagram corresponds to higher values of the angular momentum order parameter, indi-

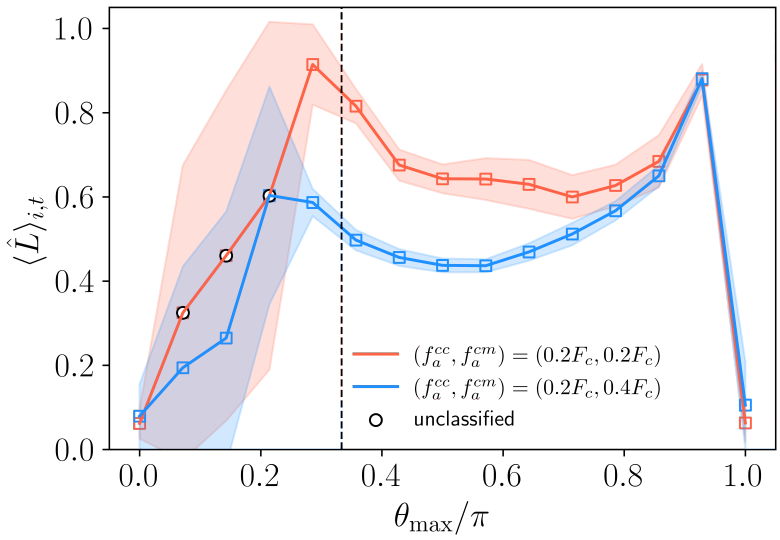

Figure A8: Impact of cell-matrix alignment on collective orbiting. All parameters are fixed except for $\theta_{\max}$ in Eq. (5), which is varied. Parameter values are taken from Section 1, with cell-matrix and cell-cell adhesion parameters chosen to represent the global (red) and peripheral orbiting (blue) regimes. Angular momentum is recorded over $t \in [200, 300]$ h and averaged across thirty simulations. Shaded regions indicate one standard deviation. The black dashed line denotes $\theta_{\max} = \pi/3$, which is the value used in the main text.

cating a global orbiting state. This may result from cell-matrix interactions dominating over active-drag forces, allowing cells to synchronize within the spheroid. Conversely, stronger self-propulsion accelerates the onset of arrest in the strong cell-cell adhesion regime.

5.3 Spheroid Size. To study how curvature and geometry influence collective orbiting, we systematically increased the spheroid radius while holding other parameters fixed (Figure A10). Increasing size reduces boundary curvature, weakening boundary detection/contact guidance and thus the synchronization needed for coherent rotation. Consequently, small (high-curvature) spheroids promote rapid, stable orbiting, whereas large (low-curvature) spheroids show decreasing coordination with impeded kinetics.

5.4 Spheroid aspect ratio. We next examined how boundary curvature impacts orbiting by imposing elliptical boundaries with sharper curvature. The orbiting state can be rapidly achieved in nearly circular domains. As the aspect ratio increases, coordinated orbiting becomes less coordinated, particularly at regions with shallower curvature. At the highest eccentricity of 0.9, the local curvature is insufficient for coordinated orbiting, since ECM

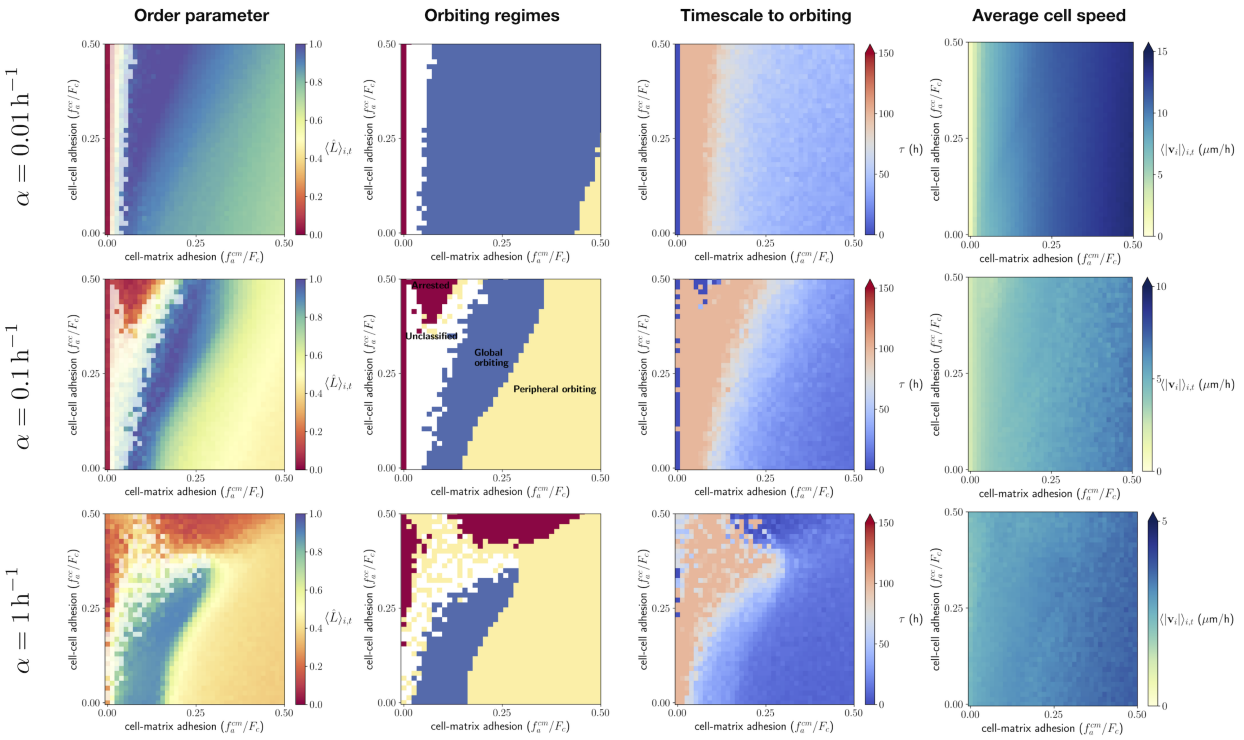

Figure A9: Impact of active-drag forces on collective orbiting. All parameters are fixed except for α (and $\beta = \alpha/u^2$ to keep u constant), which is varied. Parameter values are taken from Section 1. Angular momentum is recorded over $t \in [200, 300]$ h and averaged across fifty simulations. The columns, from left to right, represent the normalized angular momentum phase diagram, the discretized phase diagram of orbiting regimes, the timescale to orbiting (τ, Eq. (10)), and the mean cell velocity.

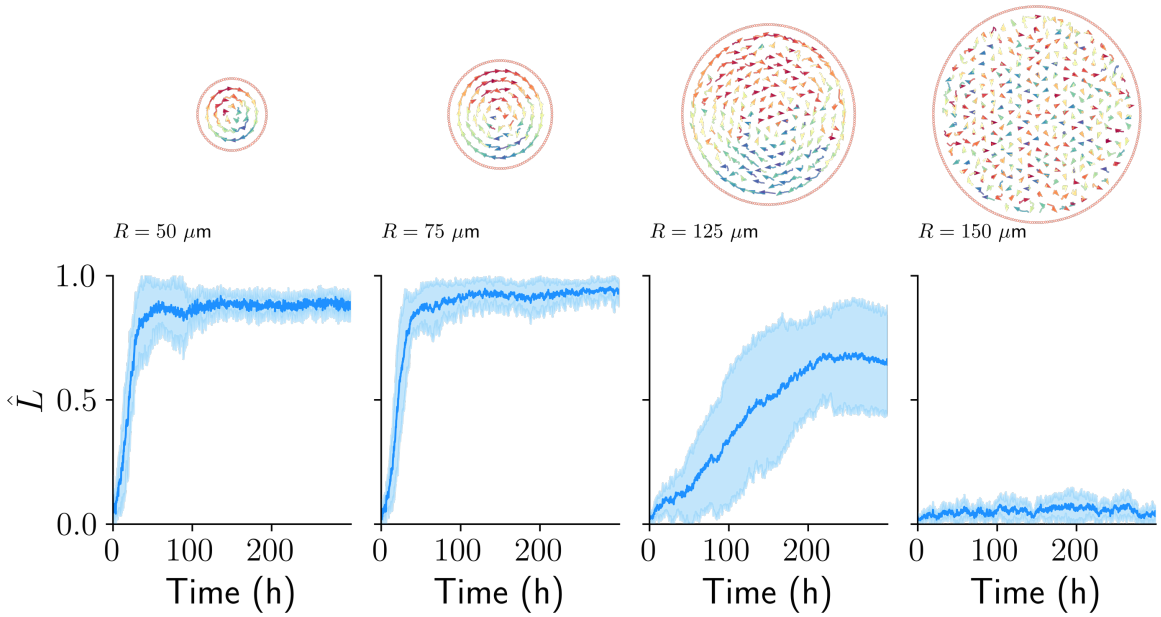

Figure A10: Effect of spheroid size on collective orbiting. Top row: snapshots of simulations for circular spheroids with increasing radius (left to right). Bottom row: normalized angular momentum about the center (mean in blue, and standard deviation across). Small spheroids (high curvature) rapidly reach a high, stable orbiting state; as size increases the rise is delayed and the plateau decreases; for the largest spheroid, the signal stays low, indicating absent or very weak orbiting over the simulation window.

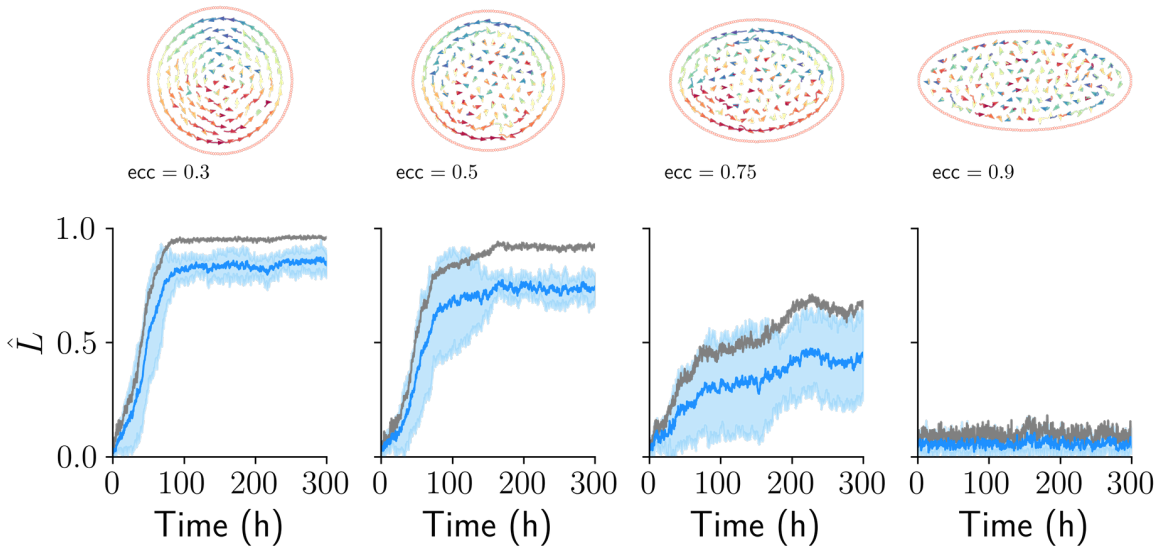

Figure A11: Effect of boundary eccentricity on the emergence of collective orbiting. Top row: simulation snapshots for concentric matrix boundaries with increasing eccentricity (while keeping total area constant). Bottom row: time courses of the normalized angular momentum about the spheroid center. Blue curves are averages (ten realizations); light-blue bands show standard deviations across simulations; gray curves show the same metric restricted to the outer layer (cells within 30 μm of the boundary). Circular domains rapidly develop robust global orbiting, while increasing eccentricity delays the onset, lowers the plateau, and ultimately delays or completely disrupts orbiting.

particles are outside of the cell's angular sensing range (Figure A11). These results indicate that regions of sharp curvature enhance boundary detection and tangential guidance at the periphery, promoting synchronized, orbiting motion.

5.5 Three boundary perturbations ($n_p = 3$). We further examined the effect of three outward-oriented Gaussian perturbations of the ECM boundary and found a similar destabilizing effect on collective orbiting as in the case of two perturbations. Beyond a critical perturbation size—approximately one cell diameter in height and two cell diameters in width—orbiting was disrupted (Fig. A12). The phase diagram closely resembles the two-perturbation case, reinforcing that multiple sharp boundary features make coordinated migration more difficult by reducing the length of continuously curved boundary available for collective motion.

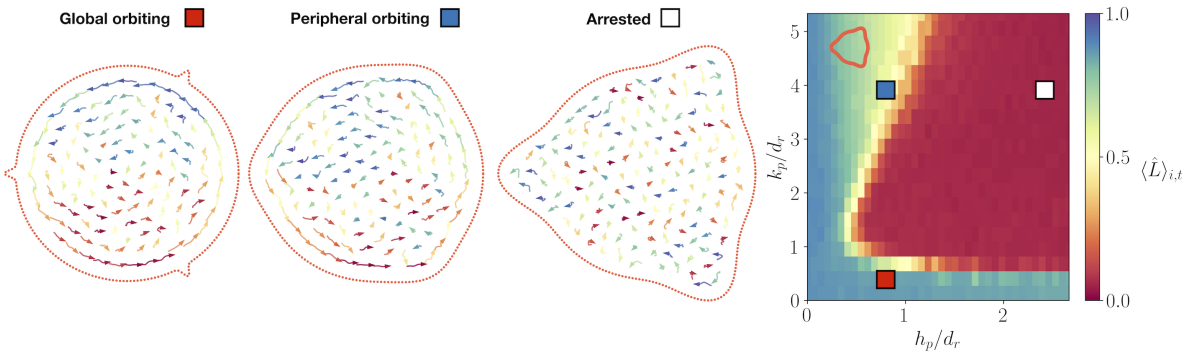

Figure A12: Orbiting is disrupted by three evenly spaced boundary perturbations. Representative snapshots of global orbiting (red square), peripheral orbiting (blue square) and arrested migration (white square) with three boundary perturbations, and the corresponding phase diagram depicting how the angular order parameter phase diagram responds to different perturbation heights and widths.

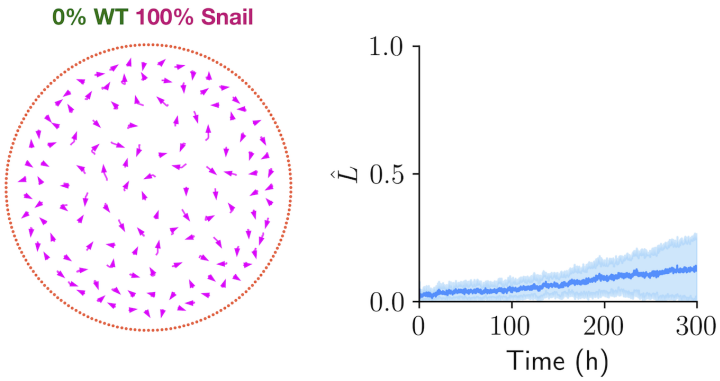

Figure A13: Spheroid composed entirely of Snail cells fails to develop stable orbiting. Left: snapshot of a circular boundary with instantaneous cell velocities. Right: normalized angular momentum over time (mean in blue, and standard deviation in shaded light blue). The signal remains low and never reaches a sustained plateau within the simulation window, indicating absent or greatly delayed, unstable orbiting.

5.6 Spheroid with 100% Snail cells. Next, and before studying mosaic spheroids, consider a spheroid composed of Snail cells (Figure A13). In these simulations, Snail cells exhibit stronger cell–matrix adhesion and negligible cell–cell adhesion. This increased adherence to the boundary promotes peripheral engagement but the isotropic matrix sensing prevents the transmission of tangential cues required for coordinated rotation, thereby suppressing orbiting. The lack of cell-cell adhesion also produces a non-uniform density profile, with cells accumulating near the periphery and a relative depletion in the core.

5.7 Differential adhesion and orbiting in two-species spheroids ($\theta^{(2)}_{\max}$). We finally investigated the case where Snail cells exhibit directionality when sensing the matrix, implemented by setting the same maximum cell-matrix alignment angle as WT cells ($\theta^{(2)}_{\max} = \theta^{(1)}_{\max} = \pi/3$). In this scenario, orbiting remains stable in mixed cell populations, as both cell types are capable of orbiting independently (Fig. A14). Interestingly, these simulations reveal classical sorting patterns driven by differential adhesion, considering both cell-cell and cell-matrix interactions. Since Snail cells exhibit weaker cell-cell adhesion but stronger cell-matrix adhesion, they preferentially localize at the boundary while maintaining peripheral orbiting. These findings highlight that disrupting orbiting requires a change in the directionality of cell-matrix interactions, as demonstrated in the main text.

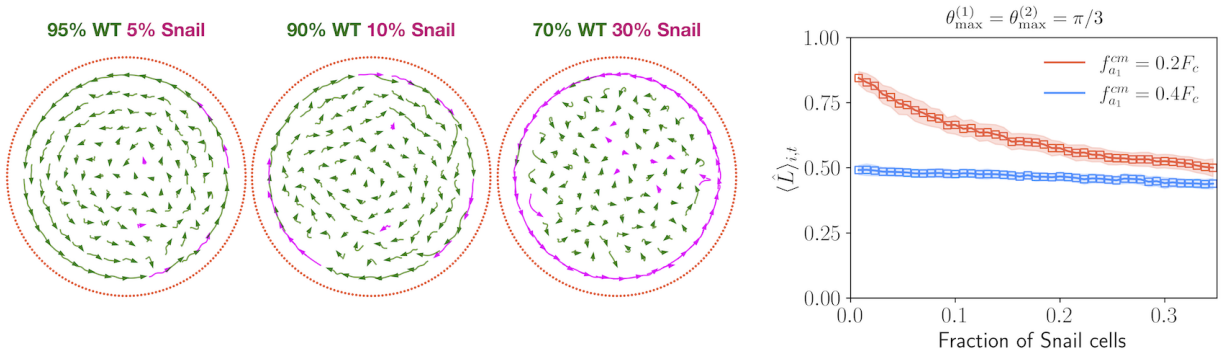

Figure A14: Orbiting and differential adhesion in two-species spheroids. (left) Representative snapshots of numerical simulations with increasing percentages of Snail populations are shown. (right) Average normalized angular momentum over the last 100 hours of the simulation as a funciton of the fraction of snail cells. Red squares denote simulations in which the cell-matrix adhesion parameter for WT cells, $f^{cm}_{a_1}$, is equal to $0.2F_c$, while blue squares indicate simulations in which the same parameter is set equal to $0.4F_c$ (see Table 2 for more details). Shaded regions indicate one standard deviation. (C) Normalized angular momentum over time (mean in blue, and standard deviation in shaded light blue) for a spheroid with 100% Snail cells. The signal remains low and never reaches a sustained plateau within the simulation window, indicating absent or greatly delayed, unstable orbiting.

References

[1] G. Albi, D. Balague, J. A. Carrillo, and J. von Brecht. Stability analysis of flock and mill rings for second order models in swarming. *SIAM Journal on Applied Mathematics*, 74(3):794, 2014.

[2] A. L. Bertozzi, T. Kolokolnikov, H. Sun, D. Uminsky, and J. v. Brecht. Ring patterns and their bifurcations in a nonlocal model of biological swarms. *Communications in Mathematical Sciences*, 13(4):955–985, 2015.

[3] J. A. Carrillo, A. Colombi, and M. Scianna. Adhesion and volume constraints via nonlocal interactions determine cell organisation and migration profiles. *Journal of Theoretical Biology*, 445:75–91, 2018.

[4] M. R. D'Orsogna, Y.-L. Chuang, A. L. Bertozzi, and L. S. Chayes. Self-propelled particles with soft-core interactions: patterns, stability, and collapse. *Physical Review Letters*, 96(10):104302, 2006.

[5] R. L. Graham, B. D. Lubachevsky, K. J. Nurmela, and P. R. Östergård. Dense packings of congruent circles in a circle. *Discrete Mathematics*, 181(1-3):139–154, 1998.